



저작자표시-비영리-변경금지 2.0 대한민국

이용자는 아래의 조건을 따르는 경우에 한하여 자유롭게

- 이 저작물을 복제, 배포, 전송, 전시, 공연 및 방송할 수 있습니다.

다음과 같은 조건을 따라야 합니다:



저작자표시. 귀하는 원저작자를 표시하여야 합니다.



비영리. 귀하는 이 저작물을 영리 목적으로 이용할 수 없습니다.



변경금지. 귀하는 이 저작물을 개작, 변형 또는 가공할 수 없습니다.

- 귀하는, 이 저작물의 재이용이나 배포의 경우, 이 저작물에 적용된 이용허락조건을 명확하게 나타내어야 합니다.
- 저작권자로부터 별도의 허가를 받으면 이러한 조건들은 적용되지 않습니다.

저작권법에 따른 이용자의 권리는 위의 내용에 의하여 영향을 받지 않습니다.

이것은 [이용허락규약\(Legal Code\)](#)을 이해하기 쉽게 요약한 것입니다.

[Disclaimer](#)

공학박사학위논문

반도체 초음파 세정 및 건조과정에서
발생하는 미세구조물 손상에 대한 연구

Study of microstructure damage in ultrasonic
cleaning and drying of semiconductors

2014년 8월

서울대학교 대학원

기계항공공학부

김태홍

반도체 초음파 세정 및 건조과정에서 발생하는 미세구조물 손상에 대한 연구

Study of microstructure damage in ultrasonic
cleaning and drying of semiconductors

지도교수 김 호 영

이 논문을 공학박사학위논문으로 제출함

2014년 5월

서울대학교 대학원
기계항공공학부
김 태 홍

김태홍의 박사학위논문을 인준함

2014년 6월

위 원 장 최 해 천 (인)
부 위 원 장 김 호 영 (인)
위 원 박 형 민 (인)
위 원 김 도 년 (인)
위 원 김 태 성 (인)

Abstract

Study of microstructure damage in ultrasonic cleaning and drying of semiconductors

Tae-Hong Kim

Department of Mechanical and Aerospace Engineering
The Graduate School
Seoul National University

In this work, we consider the interactions between microscale structures and liquid interfaces of either bubbles or evaporating films in semiconductor cleaning processes. Our particular interests lie in visualization of the microstructure damages, and construction of a stability regime map that guides us to find a process condition that avoids pattern damage in semiconductor cleaning processes.

The semiconductor cleaning process is composed of removing contaminants produced during the fabrication process using the gas bubble oscillation from ultrasounds and rinsing the cleaning solution used in the cleaning with clean water for drying. Here, the disruptive bubble behavior due to the ultrasound breaks apart structures as strong forces are applied to the microstructure as well as the contaminant particles. Also, in the drying process, pattern damage phenomenon is frequently observed where the patterns adhere to each other due to the capillary forces of the liquid. Therefore, this study was conducted

by dividing the pattern damage occurring during semiconductor cleaning as 1) the structural damage occurring during the ultrasonic cleaning due to the destructive ultrasound bubbles and 2) the clustering of microstructures due to liquid film evaporation during the drying process.

Bubble oscillations play a crucial role in ultrasonic cleaning, a process by which micro- and nanoscale contaminant particles are removed from solid surfaces, such as semiconductor wafers, photomasks and membranes. Although it is well known that the ultrasonic cleaning may damage the functional patterns of ever-shrinking size in current manufacturing technology while removing dust and debris, the mechanisms leading to such damage have been elusive. Here we report observations of the dynamics of bubbles that yield microstructure damage under a continuous ultrasonic field via high-speed imaging. We find that the bubble behavior can be classified into four types, namely volume oscillation, shape oscillation, splitting and chaotic oscillation, depending on the acoustic pressure and bubble size. This allows us to construct a regime map that can predict the bubble behavior near a wall based on the experimental parameters. Our visualization experiments reveal that damage of microwalls and microcantilevers arises due to either splitting small bubbles or chaotically oscillating large bubbles in the ultrasonic field, with the forces generated by them quantitatively measured.

As a liquid film covering an array of micro- or nanoscale pillars or walls evaporates, its meniscus straddling the microstructures pull the elastic patterns together because of surface-tension effects, leading to self-organization of slender microstructures. While this elastocapillary coalescence may provide various useful properties, such as particle-trapping and adhesion, it is detri-

mental in a semiconductor manufacturing process using a liquid film to rinse a wafer, called the spin drying. The contact of micro- and nanopatterns in semiconductor chips imply failure in the electrical circuit. To understand and find a way to prevent such phenomena, we visualize the clustering behavior of polymer micropatterns with the evaporation of liquid film while varying the sizes and temperature of the micropatterns. We find a critical role of substrate temperature in preventing the collapse of the patterns via changing the evaporation rate and behavior of the liquid film. Also, we construct a regime map that guides us to find a process condition to avoid pattern collapse in semiconductor manufacturing.

Our work provides physical understanding of interaction between micro- or nanoscale structures and liquid interfaces that are formed by either bubbles near patterns or evaporating liquid films between the patterns, and gives theoretical insights that can be applied for improving pattern damage problems in semiconductor cleaning processes.

Keywords :Pattern damage, Ultrasonic cleaning,
Microbubbles, Elastocapillary, Surface energy
Student Number : 2010-30184

Contents

Abstract	i
Contents	iv
List of Figures	vi
List of Tables	xi
1 Introduction	1
2 Disruptive bubble behavior leading to microstructure damage in an ultrasonic field	4
2.1 Introduction	4
2.2 Experiments	6
2.3 Observations of microbubble behavior	8
2.4 Observations of micropattern-damaging processes	17
2.4.1 Array of microwalls	17
2.4.2 Array of microcantilevers	20
2.5 Conclusions	26
3 Visualization and minimization of clustering of microstructures due to liquid film evaporation	29
3.1 Introduction	29
3.2 Experiments	31
3.3 The process of pattern collapse	32

CONTENTS

3.3.1	End-contact due to capillary forces during evaporation	35
3.3.2	Permanent adhesion due to surface energy after evaporation	40
3.4	The effects of substrate temperature	44
3.5	Conclusions	47
4	Concluding remarks	50
4.1	Conclusions	50
4.2	Outlook	52
	References	55
	Abstract (in Korean)	65

List of Figures

1.1	DRAM scaling trend: pattern feature sizes and aspect ratios, taken from ITRS 2012 report. The dashed line indicates that manufacturable solutions are not known.	2
1.2	Schematic illustration of typical patterning in device integration of semiconductor manufacturing processes. Solid boundary corresponds to cleaning processes.	3
2.1	(a) Experimental apparatus to image the motion of ultrasonic bubbles and the micropattern-damaging processes. (b) SEM image of a microwall array of Si. (c) SEM image of a linear array of microcantilevers of silicon.	8
2.2	Regime map of the dynamics of cavitation bubbles in ultrasonic field. When the bubble is no longer spherical under high pressure amplitude waves, we use the equivalent radius of a sphere whose area in the image is the same as that of the bubble. Error bars correspond to the standard deviations. \circ , volume oscillation; \square , shape oscillation; \triangle , splitting; \triangleright , chaotic oscillation.	10

LIST OF FIGURES

2.3	Distinct types of the dynamics of ultrasonic bubbles. (a) Volume oscillation of a bubble of $\hat{R} = 0.20$ at $\hat{P} = 29$. (b) Splitting and jetting of a bubble of $\hat{R} = 0.63$ under $\hat{P} = 29$. The magnified view at $59.3 \mu\text{s}$ reveals that the jet has not reached the lower interface of the bubble yet. (c) Shape oscillation of a bubble of $\hat{R} = 1.33$ at $\hat{P} = 45$. (d) Chaotic oscillation of a bubble of $\hat{R} = 1.04$ at $\hat{P} = 63$. (e) Evolution of the oscillation behavior of a bubble of $\hat{R} = 0.78$ with the increase of the acoustic pressure. As P_a increases from zero to \hat{P}_m , the bubble exhibits the volume oscillation (0 s), shape oscillation ($200 \mu\text{s}$), splitting ($600 \mu\text{s}$), and then chaotic oscillation ($700 \mu\text{s}$ and thereafter).	11
2.4	Splitting and jetting of ultrasonic bubbles. (a) Splitting of a small bubble of $\hat{R} = 0.13$ at $\hat{P} = 48$. (b) Jetting of a bubble of $\hat{R} = 0.74$ while \hat{P} increases to a stable value of $\hat{P} = 29$ from zero. The dents at 29.6 and $74.1 \mu\text{s}$, indicated by arrows, allow us to estimate the liquid jet speed. (c) Images of bubbles with $0.6 < \hat{R} < 0.9$ that produce liquid jets towards the wall at pressures lower than $\hat{P} = 29$	13
2.5	Shape oscillations of ultrasonic bubbles. (a) The second-mode oscillation with $\hat{R} = 0.32$ at $\hat{P} = 39$. (b) The fourth-mode oscillation with $\hat{R} = 0.80$ at $\hat{P} = 29$. (c) The fifth-mode oscillation with $\hat{R} = 1.07$ at $\hat{P} = 45$. Scale bar, $100 \mu\text{m}$. (d) The mode number versus bubble radius at the acoustic forcing frequency of 26 kHz . The circles correspond to Lamb's formula, the squares to the experimental results, and the dashed line to the model of Francescutto & Nabergoj (1978).	15

LIST OF FIGURES

2.6	<p>(a) An ultrasonic bubble undergoing volume oscillation on the silicon microwall array at $\hat{P} = 45$. (b) A bubble splitting on a Si line pattern leads to its damage at $\hat{P} = 63$. The bright region indicated by an arrow in 100 μs turns dark after destruction. An SEM image of a broken microwall is also displayed. (c) A liquid jet from dividing interfaces is directed towards the upper wall at $\hat{P} = 63$. (d) Two tiny daughter bubbles are formed by splitting and a liquid column perpendicular to both the walls is visible at $\hat{P} = 63$. (e) Periodic splitting of bubbles that forms interfaces parallel to the walls at $\hat{P} = 63$.</p>	19
2.7	<p>Destruction of microwalls due to chaotically oscillating bubbles at $\hat{P} = 63$. The arrows indicate the regions where destruction has occurred.</p>	21
2.8	<p>Deflection of microcantilevers due to ultrasonic bubbles at $P_a = 76$ kPa. (a) Schematic model. (b) Shape oscillation. (c) Splitting. (d) Chaotic oscillation. The white dashed line has been drawn to aid identification of the microcantilever. Scale bars, 200 μm</p>	23
2.9	<p>High-speed images of a chaotically oscillating bubble breaking a silicon microcantilever. (a) The chaotic oscillation can be extremely violent to lead to the cantilever fracture. The white dashed lines have been drawn to aid identification of the microcantilever. A fragment is shown at 267 μs as enclosed by an ellipse. (b) The microcantilever indicated by an arrow disappears between the images of 41.7 μs and 50.0 μs. The fragment is shown at 50.0 μs as enclosed by an ellipse. Scale bars, 200 μm.</p>	25

LIST OF FIGURES

2.10	Maximum stress at the clamped end of a cylindrical Si pillar due to the uniform pressure P exerted by microbubbles as a function of the aspect ratio, h/a	27
3.1	(a) Experimental apparatus to image the liquid film behavior in the process of pattern collapse. The upper right inset depicts the interaction of the liquid film and the pattern. (b) Cylindrical pillar array and (c) rectangular array. Scale bars, $50 \mu\text{m}$	33
3.2	The process of pattern collapse. Samples with $AR = 4$ were rinsed by IPA, and then dried at room condition. (a) Top view of cylindrical pillar array and (b) $m \times n$ rectangular array. (c) Side view of $1 \times n$ rectangular array. (d) Scanning-electron microscopy (SEM) images of collapsed pillar array and (e) rectangular array. Scale bars, $50 \mu\text{m}$	36
3.3	(a) Contact regime map : the moment ratio as a function of aspect ratio. Experimentally the patterns were collapsed in the gray regime. The superscript R , rectangular array; C , cylindrical pillar array. The half-filled symbol correspond to recovered pattern after contact each other. Previous experimental data: [1], Deguchi <i>et al.</i> (1992); [2], Tanaka <i>et al.</i> (1993); [3], Tanaka <i>et al.</i> (1994b); [4], Chandra & Yang (2010); [5], Duan & Berggren (2010); [6], Kim <i>et al.</i> (2012). (b) Top view of cylindrical pillar array with $AR = 2$ was rinsed by IPA, and that was recovered after contact. Scale bar, $50 \mu\text{m}$	39

LIST OF FIGURES

3.4	Permanent adhesion due to surface energy. (a) Schematic models of a rectangular array and (b) a cylindrical pillar array. (c) Adhesion regime map : the energy ratio as a function of aspect ratio. (d) Top view of rectangular array with $AR = 2.6$. This array was rinsed with HFE-7100, and then restored due to decreasing of contact length ($l_c/l \approx 0.47$). Scale bar, $50 \mu\text{m}$	44
3.5	Restoration of micro arrays on the high temperature substrate. The samples with $AR = 4$ were rinsed with IPA, and then dried on the high temperature substrate. (a) Top view of a cylindrical pillar array at 149°C and (b) a rectangular array at 146°C . The thin film, indicated by the arrow, trapped at the top of the pattern. (c) Side view of a rectangular array at 184°C . The dashed line has been drawn to aid identification of the substrate. Scale bars, $50 \mu\text{m}$. (d) Schematic illustration of pattern restoration. (e) Probabilities of pattern collapse as a function of pattern temperature with IPA and (f) HFE-7100.	48
3.6	Dry contact aggravates pattern collapse probability. (a) Probabilities of pattern collapse with dry air as a function of pattern temperature with IPA and (b) HFE-7100.	49
4.1	Atomic force microscope(AFM) images of a nanopillar array of silicon. (a) Top view of free-standing nanopillar array. (b) Tilted view of distorted nanopillar array. Scale bars, $1 \mu\text{m}$	53
4.2	IPA rinsing process in spin drying. IPA was injected on the thin film of water. Then the IPA repelled the water films and developed fingering of the IPA. The arrows indicate the dried areas due to IPA repulsion. Scale bar, $5 \mu\text{m}$	54

List of Tables

2.1	Measurement results of the deflection of the free end of cantilevers, δ_m , and the corresponding bubble pressure P in each oscillation mode at the constant acoustic pressure condition of $\hat{P} = 63$. We also list the characteristic velocities of liquid flows, v_d and v_h , assuming that the deflection is due to dynamic pressure and water hammer, respectively: $v_d = (P/\rho)^{1/2}$ and $v_h = P/\rho c$	23
3.1	Properties of rinse liquids; surface tension at 25°C, contact angle on a flat PDMS sample, and normal boiling point. a , taken from Product information sheet from 3M.	32
3.2	Surface energy in air and Young’s modulus of materials: a , taken from Chaudhury & Whitesides (1991); b , taken from Bauer <i>et al.</i> (1996); c , taken from Chandra & Yang (2010); d , the surface energy of bare silicon is much higher (1400 mJ m ⁻²). We used a silicon substrate with a thick oxide layer taken from Yu <i>et al.</i> (2001).	41

Chapter 1

Introduction

The most critical foundation of the modern electronics fabrication industry, the wafer can be described as an almost flat structure where numerous nano-sized patterns are accumulated in a physical perspective. With a trend of ever-shrinking feature sizes, the widths and gaps of patterns on wafer are now well below 100 nm as shown in Figure 1.1. As the design rule of semiconductor devices becomes smaller, various contaminants can contaminate the surface during the wafer fabrication process or semiconductor fabrication process for device integration (see Figure 1.2). Such contaminants on the wafer, however small, can cause malfunctioning of the complex micro-electromechanical systems (MEMS), reducing the overall semiconductor device production yield rate. Thus, cleaning needs to be conducted to lower the contaminant concentration to specific levels. Through the serial processes of contaminant removal and drying, the cleaning solution used for wafer cleaning has to be removed.

Ultrasonic cleaning processes conduct acoustic excitation beyond the audible frequency range within the liquid to induce sound pressure variability. This sound pressure removes fine dust using the motion of the cavitation bubbles generated, and the movement of the bubbles play an important role in particle removal. However, as the size of the microstruc-

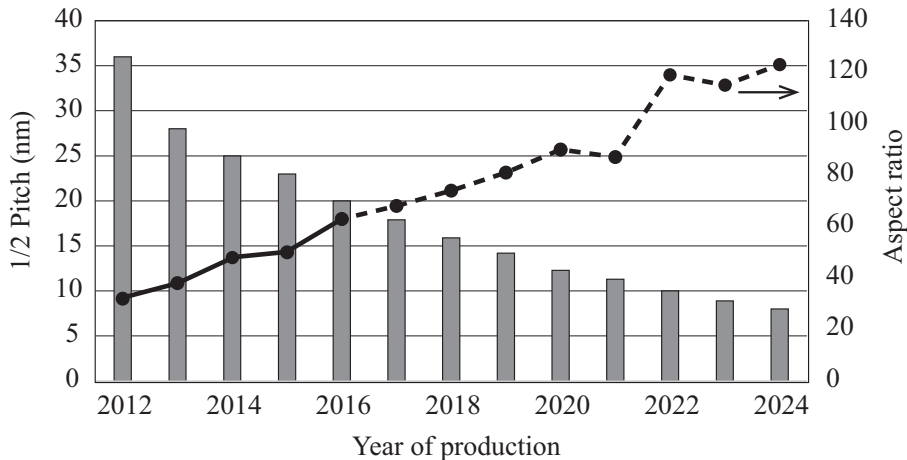


Figure 1.1: DRAM scaling trend: pattern feature sizes and aspect ratios, taken from ITRS 2012 report. The dashed line indicates that manufacturable solutions are not known.

As pattern feature sizes become smaller and smaller, the structures themselves are found to break apart as the bubble oscillation applies great force. Therefore, the principle of removing the contaminant particles as well as the principle behind the destruction of the microstructures due to the bubbles need to be understood to find a method enhancing the contaminant removal efficiency and minimizing microstructure damage.

Also, the amount of liquid film and the height gradually decreases due to the evaporation of the liquid completely covering the wafer in the drying processes. Before the liquid is completely removed, the liquid film drapes at the pattern ends. Here, the capillary forces existing between the liquid film and the solid structure pulls on the pattern and permanent damage can result when the deformation of the elastic structure goes beyond a specific degree. Although capillary force is small compared to gravitational force in a macro scale, capillary force is relatively significant in very small scales. The patterns on a wafer approximately range from the micrometers to the nanometers, thus, the capillary force of the cleaning solution can be

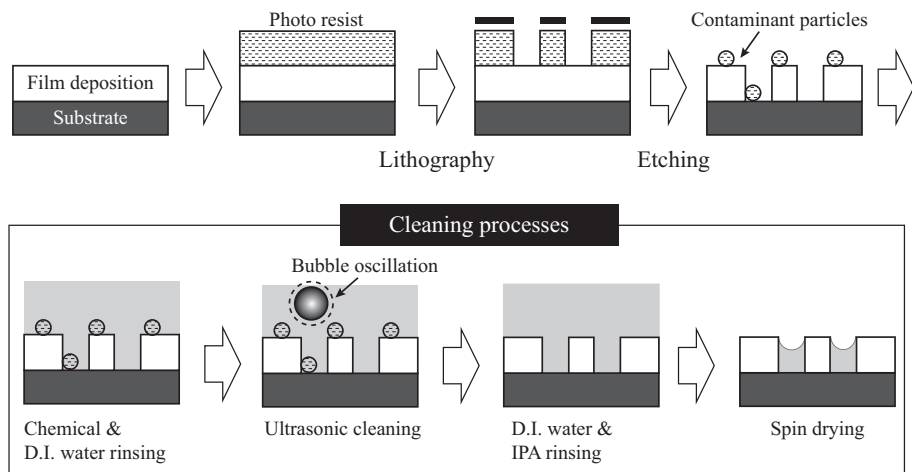


Figure 1.2: Schematic illustration of typical patterning in device integration of semiconductor manufacturing processes. Solid boundary corresponds to cleaning processes.

a significant force to the patterns. Hence, cases of the patterns remaining intact during the particle removal process but being permanently damaged during the drying process are frequently observed in the conventional drying process, causing numerous problems. Up to now, most microstructure damage minimization studies varied the process conditions without direct observation of the cleaning processes or focused on defining the damage principle of the microstructure using macroscopic laws of physics.

Thus, in this study, microstructure damages during the ultrasonic cleaning and drying processes were visualized to reveal the principle behind the microstructure damage. Furthermore, a simple theoretical model was developed to investigate methods for structure damage minimization.

Chapter 2

Disruptive bubble behavior leading to microstructure damage in an ultrasonic field

2.1 Introduction

Ultrasound traveling through a liquid produces pressure waves, which cause negative pressure during the rarefaction stage. This negative pressure may lead to cavitation from pre-existing nuclei of dissolved gas as well as the rupture of the fluid (Leighton, 1994; Wagterveld *et al.*, 2011). The cavitation bubbles oscillate under the continuous ultrasonic excitations, thereby generating a pressure gradient between the far-field fluid and the bubble surface (Kim *et al.*, 2009). They also translate due to the primary Bjerknes force while interacting with each other through the secondary Bjerknes force (Crum, 1975; Mettin *et al.*, 1997). The local fluid motions induced by oscillating bubbles that undergo translation can be responsible for the cleaning of contaminant particles from solid surfaces (Gonzalez-Avila *et al.*,

This chapter has been published as (Kim & Kim, 2014)

2011; Kim *et al.*, 2009). Ultrasonic cleaning processes are widely employed for cleaning of photomasks and wafers in semiconductor industries, surgical instruments, and membranes (Lamminen *et al.*, 2004). The cleaning efficiency, often measured by the particle removal efficiency (Busnaina & Gale, 1997), increases with the acoustic pressure amplitude. It is because bubble mobility enhanced by high acoustic pressure leads to increased particle-detachment forces and allows wider area to be swept by ultrasonic bubbles. However, it is well known that strong ultrasonic pressure waves lead to the damage of solid surfaces as well as the removal of contaminant particles (Holsteyns *et al.*, 2005; Kim *et al.*, 2010). Pits and holes on fragile substrates (Chen *et al.*, 2006; Wagterveld *et al.*, 2011) and broken patterns on semiconductor chips (Tomita *et al.*, 2009) were observed after ultrasonically cleaning the surfaces, but the dynamic behavior of ultrasonic bubbles leading to such damages has been seldom captured.

Cavitation bubbles induced by electric sparks or laser pulses have been mainly so far used to investigate the interaction of bubbles with a solid wall. Unlike ultrasonic bubbles, they can be introduced into the liquid at a precisely known size and location, which greatly facilitates the experimental observation. However, the dynamics of cavitation bubbles under continuous acoustic wave field that are actually used in ultrasonic cleaning are different from those under the impulse by spark or laser. Impulsively generated cavitation bubbles are filled with vapour produced by plasma recombination and thus have a few microseconds of life time (Lauterborn & Hentschel, 1985). They initially expand explosively and then perish after a few rebound cycles. Dynamic behaviors of the spark- or laser-induced bubbles were classified based on the relative distance between the bubble and the solid surface to the maximum bubble radius (Lindau & Lauterborn, 2003; Shima *et al.*, 1983; Vogel *et al.*, 1989). The dents formed by those bubbles on soft substrates were reported (Brujan *et al.*, 2001; Philipp & Lauterborn, 1998; Tomita & Shima, 1986), revealing the disruptive capa-

bility of those bubbles. On the other hand, the acoustic cavitation bubbles under continuous waves are filled with gases dissolved in liquid, and respond periodically to driving acoustic waves with a considerably long life time (Lauterborn & Ohl, 1997). Because of inherent difficulties in predicting the location of individual bubbles, the interaction of the ultrasonic bubbles with solid structures has been scarcely observed thus far in contrast to that of the spark- or laser-induced bubbles.

Therefore, here we aim to overcome the difficulties in capturing the dynamic behavior of individual ultrasonic bubbles and analyze the interface motions and interaction with solid structures. Through the observation, we elucidate the mechanisms that result in the damage of solid structures due to ultrasonic bubbles. In the following, we first describe the experimental apparatus and technique employed in this work. We then report different types of bubble behaviors, which lead to a regime map characteristic of ultrasonic bubbles. We finally visualize the pattern-damaging process to find the disruptive mechanisms of ultrasonic bubbles that are different from those of the spark- or laser-induced bubbles.

2.2 Experiments

We use the apparatus as shown in figure 3.1 to visualize the microbubble motion under continuous ultrasonic waves. The setup consists of a stainless steel bath on one of whose side a piezoelectric transducer vibrating at 26 kHz is attached, an upright microscope (Olympus BX-51M) with a water immersion objective lens (Olympus LUMPLFL 10XW or 40XW), and a high-speed camera (Photron SA1.1). The high-speed camera runs at a frame rate of up to 120 kHz, which can take approximately 4-5 images of the bubble motion within a single ultrasonic period. It was ensured that the entire transient interface motion was recorded by the image sensor by setting the exposure time to be equal to $1/120000$ s when the frame rate was 120 kHz. That is, no matter how fast the interfacial motion may

2.2 Experiments

be, its trace should be captured because the camera shutter is open. Distilled water with 7 mg of O_2 per litre at room temperature as measured by an oxygen sensor (Unisense OX-100) is used as the liquid medium. As solid walls interacting with bubbles, we use a polyimide substrate, an array of microwalls patterned on a silicon wafer, and microcantilevers. A silicon microwall array of 3.7, 2.5 and 10.6 μm in height, width and spacing, respectively, is fabricated by deep reactive ion etching. A linear array of silicon cantilever beams of 15, 130 and 3 μm in width (w), length (l) and thickness (b), respectively, is used to observe their deflections due to forces generated by bubble oscillations. Figures 3.1(*b,c*) shows the scanning electron microscopy (SEM) images of the microwall array and the microcantilevers. The acoustic pressure amplitude, P_a , whose root mean square (RMS) value can be sustained at a constant by the amplifier driving the piezoelectric transducer ranges from 35 to 76 kPa, as measured by a needle hydrophone (Precision Acoustics HPM1/1). We use the RMS values of the pressure because it fluctuates naturally due to finite near-field effects, reflections from the wall, and absorption and scattering of acoustic waves by cavitation bubbles.

While the location and size of bubbles generated by a spark or laser can be precisely controlled, it is impossible to predict when and where individual bubbles will emerge and interact with a solid boundary under ultrasonic waves. Numerous cavitation bubbles that are generated ultrasonically move around rapidly due to the primary and secondary Bjerknes forces and acoustic streaming. However, we succeeded in capturing the moments individual bubbles interact with the solid wall by continually observing a selected area under the microscope until a bubble appears. Then the high-speed camera saves the images stored in the memory before and after the triggering moment. We present the visualization results of the dynamics of ultrasonic bubbles and their interaction with solid walls in the following.

2.3 Observations of microbubble behavior

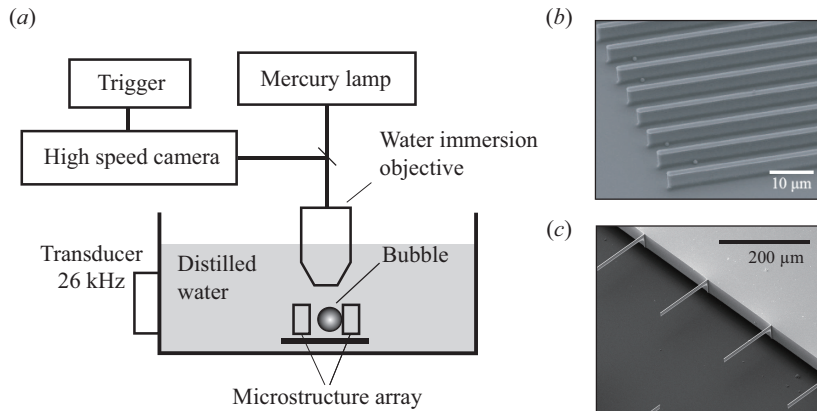


Figure 2.1: (a) Experimental apparatus to image the motion of ultrasonic bubbles and the micropattern-damaging processes. (b) SEM image of a microwall array of Si. (c) SEM image of a linear array of microcantilevers of silicon.

2.3 Observations of microbubble behavior

We start with the dynamic behavior of a single microbubble near a rigid solid wall, a polyimide substrate in our case. In the ultrasonic field, bubbles of a wide size range are generated and oscillate. Thus, we observe how bubbles of various sizes respond to different acoustic pressure amplitudes that are controlled by the amplifier and measured by the hydrophone. These experiments allow us to construct a regime map to classify the behavior of ultrasonic bubbles depending on the bubble size and the acoustic pressure amplitude. We find four distinct types of bubble behavior near a solid wall, which we refer to as volume oscillation, shape oscillation, splitting, and chaotic oscillation. To find dimensionless parameters that identify the conditions in which each behavior arises, we first consider the resonance radius of a cavitation bubble in the ultrasonic field. For a bubble undergoing harmonic radial oscillation within an inviscid liquid, the linear resonance angular frequency, ω_r , is given by the Minnaert formula (Minnaert, 1933), $\omega_r = (3\kappa P_0/\rho)^{1/2}/R_r$, where κ is the adiabatic exponent (1.4

2.3 Observations of microbubble behavior

for air bubble), P_0 is the ambient pressure, ρ is the liquid density, and R_r is the nominal radius of the bubble at rest. Therefore, the resonance bubble radius corresponding to the ultrasonic frequency 26 kHz for water at $P_0 = 1$ atm is $R_r = 124 \mu\text{m}$. This bubble radius allows us to find the characteristic pressure of the interior of a bubble at rest with respect to the outer pressure using the Laplace formula: $P_r = 2\sigma/R_r = 1.2$ kPa, where σ is the surface tension coefficient between water and air. Using the time-averaged bubble radius scaled by the resonance radius, $\hat{R} = R_a/R_r$, and the acoustic pressure amplitude scaled by the Laplace pressure, $\hat{P} = P_a/P_r$, we obtain the regime map as shown in figure 2.2. Below we delineate the bubble behavior in each regime.

At a low pressure amplitude, $\hat{P} = 29$, small bubbles with $\hat{R} < 0.5$ oscillate in radius as shown in figure 2.3(a). This volume oscillation mode occurs in the lower left region in figure 2.2. For very small bubbles with $\hat{R} = 0.13$, the volume oscillation is observed up to the acoustic pressure of $\hat{P} = 45$. We write the scaled magnitude of radial oscillation as $\varepsilon = (R_1 - R_2)/(2R_a)$, where R_1 and R_2 are the maximum and minimum radius of the bubble, respectively. At a low pressure of $\hat{P} = 29$, small bubbles with $\hat{R} = 0.16$ respond periodically with $\varepsilon = 0.12$ while ε decreases to 0.05 for large bubbles with $\hat{R} = 0.43$ and 0.5. The volume oscillation becomes stronger as the acoustic pressure increases, so that a bubble with $\hat{R} = 0.13$ vibrates in radius with $\varepsilon = 0.14$ for $\hat{P} = 45$. Further increase of the acoustic pressure qualitatively changes the response of the bubble from the volume oscillation to the splitting behavior.

As P_a increases, small bubbles with $\hat{R} = 0.13$ split up into two daughter bubbles as shown in figures 2.3(b) and 2.4. This splitting behavior corresponds to the upper left region in figure 2.2. For these small bubbles, the periodic oscillation of a mode higher than the zeroth mode (volume oscillation) is seldom observed supposedly because of a great difference of the excitation frequency (26 kHz) and the natural frequency for shape oscillations.

2.3 Observations of microbubble behavior

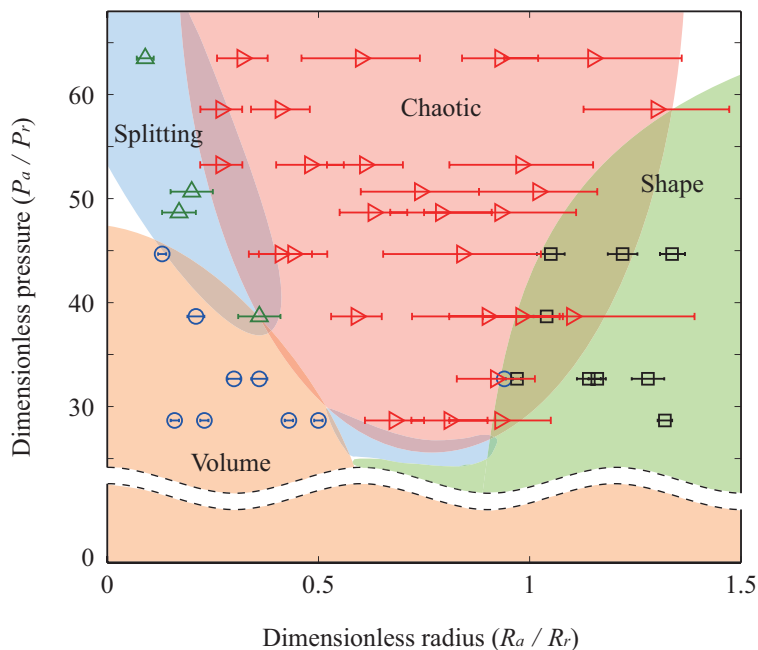


Figure 2.2: Regime map of the dynamics of cavitation bubbles in ultrasonic field. When the bubble is no longer spherical under high pressure amplitude waves, we use the equivalent radius of a sphere whose area in the image is the same as that of the bubble. Error bars correspond to the standard deviations. ○, volume oscillation; □, shape oscillation; △, splitting; ▷, chaotic oscillation.

2.3 Observations of microbubble behavior

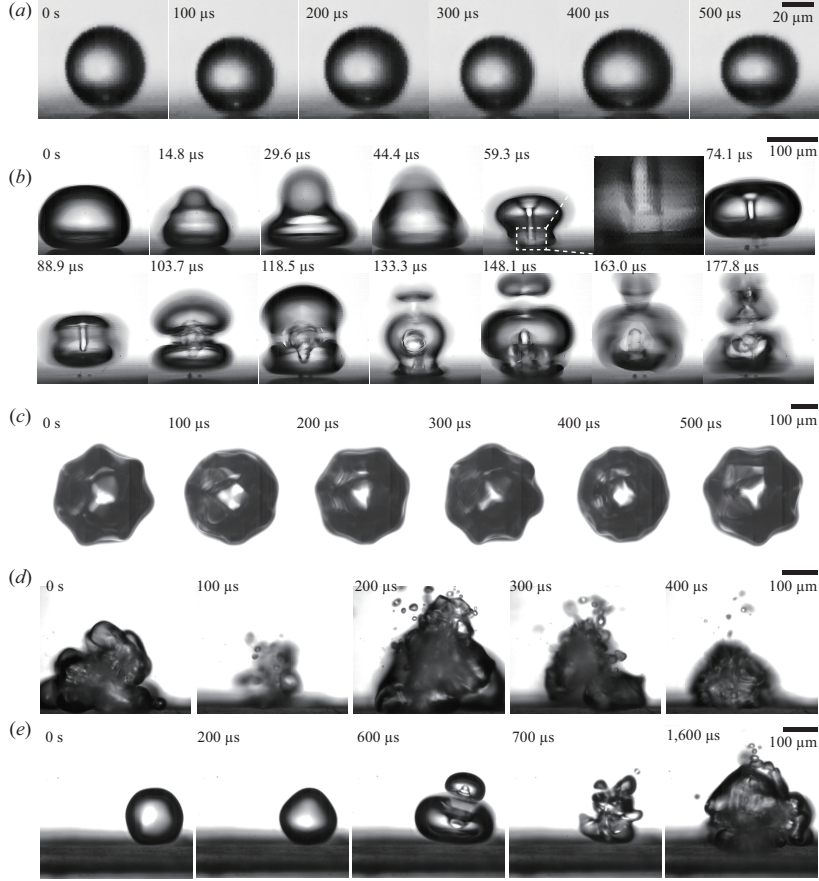


Figure 2.3: Distinct types of the dynamics of ultrasonic bubbles. (a) Volume oscillation of a bubble of $\hat{R} = 0.20$ at $\hat{P} = 29$. (b) Splitting and jetting of a bubble of $\hat{R} = 0.63$ under $\hat{P} = 29$. The magnified view at $59.3 \mu\text{s}$ reveals that the jet has not reached the lower interface of the bubble yet. (c) Shape oscillation of a bubble of $\hat{R} = 1.33$ at $\hat{P} = 45$. (d) Chaotic oscillation of a bubble of $\hat{R} = 1.04$ at $\hat{P} = 63$. (e) Evolution of the oscillation behavior of a bubble of $\hat{R} = 0.78$ with the increase of the acoustic pressure. As P_a increases from zero to \hat{P}_m , the bubble exhibits the volume oscillation (0 s), shape oscillation ($200 \mu\text{s}$), splitting ($600 \mu\text{s}$), and then chaotic oscillation ($700 \mu\text{s}$ and thereafter).

2.3 Observations of microbubble behavior

For example, the Lamb frequency for the second mode ($n = 2$) oscillation of a bubble with $\hat{R} = 0.13$ is $f_2 = (2\pi)^{-1}[(n+1)(n-1)(n+2)\sigma/(\rho R_a^3)]^{1/2} = 68$ kHz (Lamb, 1993). It was reported that the threshold pressure amplitude over which the second-mode shape oscillation occurs increases with the decrease of the bubble radius (Versluis *et al.*, 2010). In our experiments, the higher-mode oscillations last only a few ms, if any, before the bubbles are split, implying that the strong acoustic energy imparted on a small bubble with an increased P_a is released dominantly through the rapid break-up of bubble interfaces. The dents on both the interfaces of daughter bubbles are visible, $103.7 \mu\text{s}$ in figure 2.3(b) and $600 \mu\text{s}$ in figure 2.3(e). Upon the neck that connects the two daughter bubbles being pinched off, their interfaces are locally invaded by the liquid jet, leading to the dents (Brujan *et al.*, 2001). The liquid jet following this splitting process is different from the jet observed in the spark- or laser-induced bubbles near a solid wall, which is due to asymmetric collapse of a bubble (Benjamin & Ellis, 1966; Vogel *et al.*, 1989). We find that in ultrasonic bubbles, both types of the liquid jet can arise - at $74.1 \mu\text{s}$ in figure 2.3(b) is shown the liquid jets induced by asymmetric collapse of a bubble, whereas the jet following the interface split is shown at $118.5 \mu\text{s}$ in figure 2.3(b) and at $600 \mu\text{s}$ in figure 2.3(e).

We use figures 2.3(b) and 2.4(b) to deduce the velocity of the jet towards the solid wall. In figure 2.3(b), assuming that the apex of the bubble at $44.4 \mu\text{s}$ travels down to the tip of the jet at $59.3 \mu\text{s}$, the jet velocity is approximately 8.8 m s^{-1} . In figure 2.4(b), measuring the distance between the dents at $29.6 \mu\text{s}$ and $74.1 \mu\text{s}$ allows us to estimate the jet velocity to range from 2 to 3 m s^{-1} . Although these methods may give the lower bound of the jet speed, the values are in agreement with the previous measurements of jet speeds for ultrasonic bubbles by Crum (1979) and Prabowo & Ohl (2011). The fact that the liquid jets are frequently captured before they completely penetrate the lower interface of the bubble, $59.3 \mu\text{s}$ and $118.5 \mu\text{s}$ in figure 2.3(b) and $74.1 \mu\text{s}$ in figure 2.4(b), indicates that the jet speed,

2.3 Observations of microbubble behavior

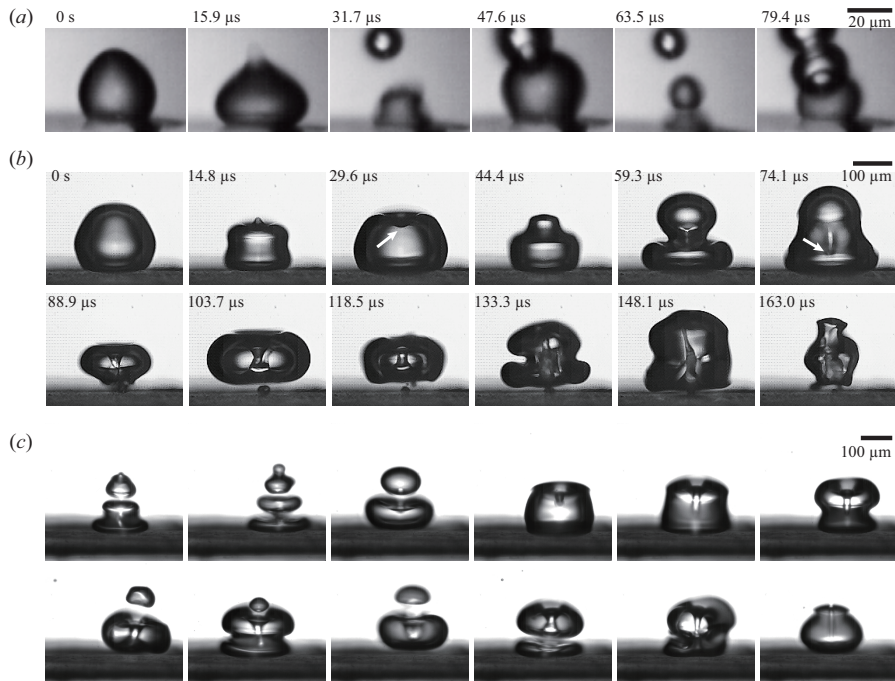


Figure 2.4: Splitting and jetting of ultrasonic bubbles. (a) Splitting of a small bubble of $\hat{R} = 0.13$ at $\hat{P} = 48$. (b) Jetting of a bubble of $\hat{R} = 0.74$ while \hat{P} increases to a stable value of $\hat{P} = 29$ from zero. The dents at 29.6 and $74.1 \mu\text{s}$, indicated by arrows, allow us to estimate the liquid jet speed. (c) Images of bubbles with $0.6 < \hat{R} < 0.9$ that produce liquid jets towards the wall at pressures lower than $\hat{P} = 29$.

2.3 Observations of microbubble behavior

v_j , is unlikely to be fast enough to travel the bubble size within the duration of a single frame, i.e. $v_j < \sim 16.5 \text{ m s}^{-1}$. The estimated jet speeds are significantly lower than the values, on the order of 100 m s^{-1} , reported for the jet induced by asymmetrical collapse of an impulsively generated bubble near a solid wall (Philipp & Lauterborn, 1998; Tomita & Shima, 1986; Vogel *et al.*, 1989). Furthermore, Prabowo & Ohl (2011) argued that break-up of the liquid jet before its penetration of the bubble weakens the impact of the jet on the substrate. The stagnation pressure of the jet that can be estimated as $P_s \sim \frac{1}{2}\rho v_j^2$, where v_j is the jet velocity, is of the order of 10 kPa. The viscous stress that is scaled as $\tau \sim \mu v_j / \delta$ (Dijkink & Ohl, 2008), where μ is the water viscosity and δ is the characteristic distance of the jet from the solid boundary, ranges in the order of 1 kPa.

Large bubbles of $\hat{R} > \sim 1$ exhibit shape oscillations as shown in figure 2.3(c) at $\hat{P} = 45$. In figure 2.2, the shape oscillation mode occurs in the lower right region. For large bubbles, the interface between the dense liquid and less dense gas phase is strongly accelerated into the bubble as P_a increases, so that the growth of initially small perturbations of volume oscillation leads to shape oscillation (Eller & Crum, 2005; Holt & Gaitan, 1996). Figures 2.5(a-c) show the shape oscillation of different sizes of bubbles. We see that the shape mode number increases with the bubble size at the fixed ultrasonic frequency, 26 kHz. Figure 2.5(d) plots the mode number versus the bubble size. The experimentally measured mode numbers of the bubbles increase almost linearly with the bubble size, but still lower than the values predicted by Lamb's formula that is supposed to hold for bubbles oscillating in an inviscid liquid. Francescutto & Nabergoj (1978) predicted the pulsation amplitude threshold for the onset of surface waves of different mode numbers on free bubbles within a slightly viscous liquid. Although a bubble in the present experiment is close to a wall and thus requires consideration of a mirror bubble and bubble-bubble interactions for rigorous theoretical analysis, we find that the most easily excitable

2.3 Observations of microbubble behavior

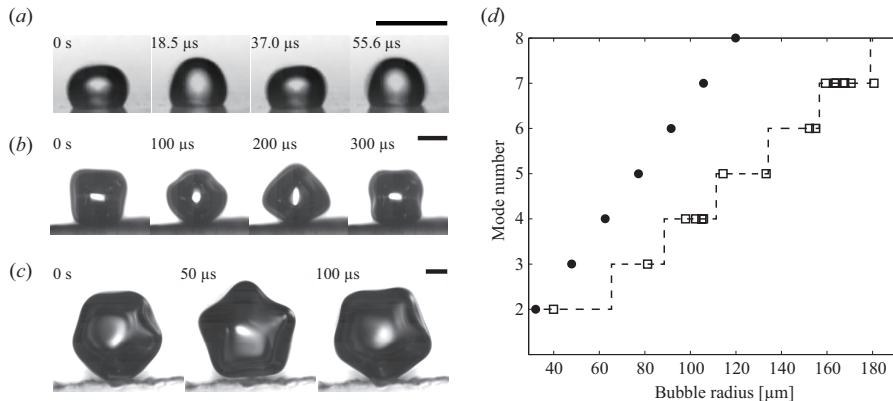


Figure 2.5: Shape oscillations of ultrasonic bubbles. (a) The second-mode oscillation with $\hat{R} = 0.32$ at $\hat{P} = 39$. (b) The fourth-mode oscillation with $\hat{R} = 0.80$ at $\hat{P} = 29$. (c) The fifth-mode oscillation with $\hat{R} = 1.07$ at $\hat{P} = 45$. Scale bar, $100 \mu\text{m}$. (d) The mode number versus bubble radius at the acoustic forcing frequency of 26 kHz. The circles correspond to Lamb's formula, the squares to the experimental results, and the dashed line to the model of Francescutto & Nabergoj (1978).

mode number as a function of the bubble radius is in agreement with the model of Francescutto & Nabergoj as shown in figure 2.5(d). A further study is called for to explain this agreement of the free bubble model and the experimental results of bubbles near the wall.

The shape oscillations of the bubbles turn extremely violent as \hat{P} increases as shown in figure 2.3(d), which we refer to as the chaotic oscillation. It is characterized by ejection of multiple daughter bubbles and the consequent formation of multiple dents distributed randomly over the bubble interface as well as by irregular but vigorous distortions of the bubble interface. The chaotic regime is located in the center of figure 2.2. In this regime, the strong acoustic energy imparted on a large bubble is released by rapid motion of corrugated interfacial areas, and partly converted to surface and kinetic energy of daughter bubbles. Previous research that used high-intensity ultrasounds termed the chaotically oscillating bubble as a cloud

2.3 Observations of microbubble behavior

bubble or bubble cluster, and reported emission of light or shock waves due to interaction of multiple bubbles (Brujan *et al.*, 2011; Chen *et al.*, 2009; Lauterborn & Ohl, 1997).

Bubbles slightly smaller than the resonance size of a freely oscillating bubble, $\hat{R} \approx 0.6 - 0.9$, are always found to exhibit chaotic oscillation under the stable acoustic pressure amplitude condition allowed in our setup, whose minimum is $\hat{P}_m = 29$. However, it is possible to observe the evolution of the bubble dynamics for $\hat{R} \approx 0.6 - 0.9$ as the acoustic pressure increases from zero to \hat{P}_m upon switching the amplifier on. As shown in figure 2.3(e), the foregoing three modes of bubble behavior, volume oscillation, shape oscillation and splitting, arise sequentially with the increase of the pressure amplitude. In particular, liquid jets are frequently observed for the bubbles of this size range as shown in the third frame of figure 2.3(e) and figure 2.4(c). In contrast, very small bubbles ($\hat{R} < 0.4$) require very strong acoustic pressure to give rise to liquid jets (Zhong *et al.* 1999; Brujan *et al.* 2011). The fact that the size range of bubbles easily prone to chaotic oscillations is shifted to the values smaller than unity ($\hat{R} = 0.6 - 0.9$) can be explained using a formula for the resonance frequency of a bubble adjacent to a wall, f_r , as suggested by Strasberg (1953): $f_r/f_{r0} = [1 + (R/2d) - (R/2d)^4]^{-1/2}$. Here f_0 is the resonance frequency of a freely oscillating bubble, R is the nominal radius of the bubble and d is the distance of the bubble center to the wall. The relationship implies that the presence of a wall decreases the resonance frequency of a bubble of a given radius, or equivalently, decreases the resonance radius at a given frequency because we may write $R_r/R_0 = [1 + (R/2d) - (R/2d)^4]^{-1/2}$, where R_r and R_0 are the resonance radii of a bubble near a wall and of a freely oscillating bubble, respectively (Dollet *et al.* 2008). For a bubble barely touching the wall, $R = d$, we get $R_r/R_0 \approx 0.8$, in good agreement with the size range of bubbles easily prone to chaotic responses in figure 2.2.

2.4 Observations of micropattern-damaging processes

The damages of solid substrates due to impulsively generated bubbles have been explained by either the high-speed liquid jet directed towards the solid wall (Benjamin & Ellis, 1966; Kornfeld & Suvorov, 1944; Naude & Ellis, 1961) or the emission of shock wave from the expanding bubble (Hickling & Plesset, 2004; Shutler & Mesler, 1965). The speed of the liquid jet induced by asymmetrical collapse of an impulsively generated bubble near a solid wall was measured to reach the order of 100 m s^{-1} as mentioned in §3. The corresponding water hammer pressure, $P_h \sim \rho c v_j$, where c is the speed of sound in water, reaches about 0.1 GPa. However, the experimentally measured speed of liquid jet formed by the splitting of ultrasonic bubbles in figure 2.3(b) is of the order of 1 m s^{-1} . Thus, the water hammer effect is negligible, lowering the possibility that the low-velocity jet of ultrasonic bubbles should damage the solid substrate. The shock wave was observed to be emitted from an impulsively generated bubble that re-expands after the collapsing phase in which the bubble content is strongly compressed (Ohl *et al.*, 1999; Shaw & Spelt, 2010; Tomita & Shima, 1986). The pressure from the shock wave was estimated to be as high as 1 GPa (Brujan *et al.*, 2011; Pecha & Gompf, 2000), a value high enough to damage solid substrates (Suwito *et al.*, 1999). For ultrasonic bubbles, however, such an explosive growth is unlikely because of periodically imposed acoustic waves. In the following, we present the high-speed imaging results of ultrasonic bubbles damaging micropatterns, such as microwalls and microcantilevers.

2.4.1 Array of microwalls

We first use an array of microwalls on a silicon wafer as a solid substrate to observe ultrasonic bubbles damage microstructures. Figure 2.6

2.4 Observations of micropattern-damaging processes

shows the interaction of small bubbles ($\hat{R} < 0.5$) with the microstructures. Since no pattern damage arises for bubbles undergoing volume oscillations as shown in figure 2.6(a), we focus on the images of the bubbles that split due to ultrasonic waves. Figure 2.6(b) shows that the wall breaks where a microbubble splits (200 μ s). An SEM image of the broken wall is also shown in figure 2.6(b). This is the first experimental evidence that splitting ultrasonic bubbles can damage microstructures, to the authors' knowledge. However, not all the splitting bubbles damage microstructures, but rather, the bubble split should occur over the microstructure to induce its damage. Figures 2.6(c-e) show that when the splitting bubbles are confined between the microwalls, the walls are hardly destroyed. Figures 2.6(c-d) show that the liquid jets or pressure wave from dividing interfaces directed perpendicular to the wall surface cannot break the microwalls. When the interface division is parallel to the wall, figure 2.6(e), neither the liquid jet nor the kinetic energy of the divided bubbles pushing the wall can cause damages.

We now estimate the magnitude of force that leads to a damage of the microwall as shown in figure 2.6(b). When a bubble overlies the microwall, the wall under the constant pressure P experiences the maximum stress at the clamped bottom, $\sigma_m = 3Ph^2/w^2$, where h and w are the height and thickness of the wall, respectively (Timoshenko & Goodier, 1970). For σ_m to reach the ultimate strength of an etched single crystalline silicon, $\sigma_u \sim 1$ GPa (Suwito *et al.*, 1999), the pressure needs to reach 152 MPa. Since the dynamic pressure generated by the liquid jet issuing from the splitting bubble is too low (of the order of 10 kPa) as discussed in §3, we are naturally led to assume that such a high pressure is caused by the shock emitted from the splitting interface. The impulsive pressure due to shock wave from a splitting spark-induced bubble confined within a narrow gap between flat plates was shown to damage solid structures by Ishida *et al.* (Ishida *et al.*, 2001). The pressure exerted on the microwall due to shock is estimated as a water hammer pressure, $P_h \sim \rho v_s c$, where v_s is the velocity of a liquid

2.4 Observations of micropattern-damaging processes

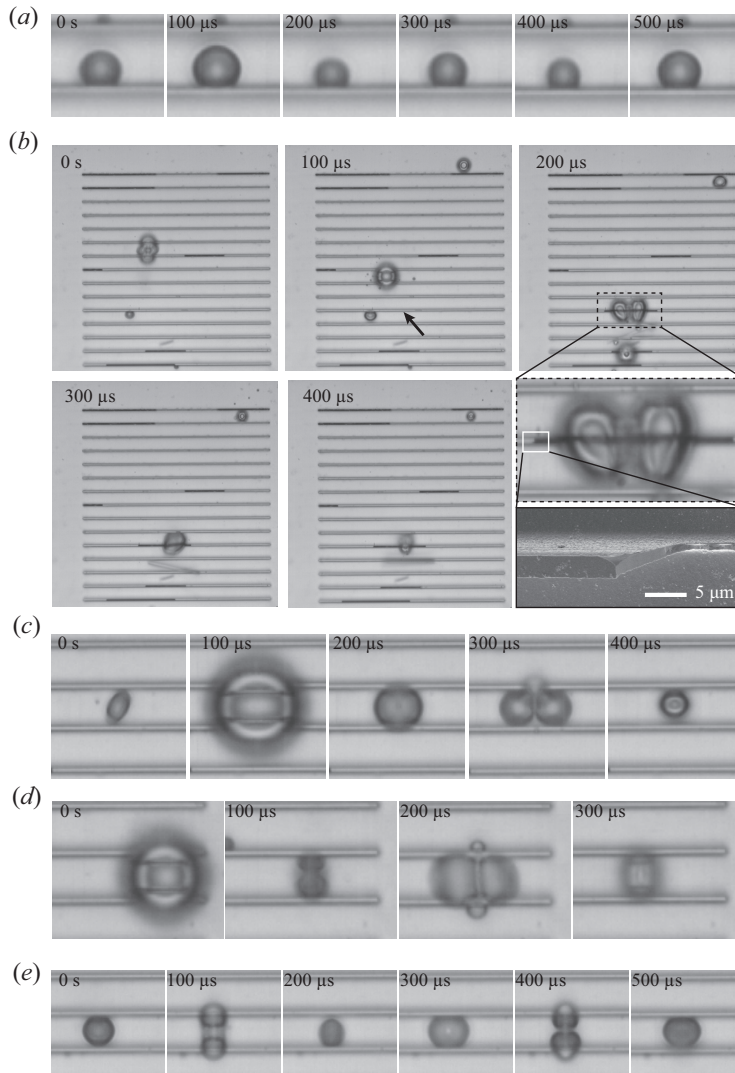


Figure 2.6: (a) An ultrasonic bubble undergoing volume oscillation on the silicon microwall array at $\hat{P} = 45$. (b) A bubble splitting on a Si line pattern leads to its damage at $\hat{P} = 63$. The bright region indicated by an arrow in $100 \mu\text{s}$ turns dark after destruction. An SEM image of a broken microwall is also displayed. (c) A liquid jet from dividing interfaces is directed towards the upper wall at $\hat{P} = 63$. (d) Two tiny daughter bubbles are formed by splitting and a liquid column perpendicular to both the walls is visible at $\hat{P} = 63$. (e) Periodic splitting of bubbles that forms interfaces parallel to the walls at $\hat{P} = 63$.

2.4 Observations of micropattern-damaging processes

flow stemming from bubble split. For P_h to reach 152 MPa, v_s should be 100 m s^{-1} . Taking this velocity as a characteristic split speed of a $100 \text{ }\mu\text{m}$ -radius bubble, it takes only $1 \text{ }\mu\text{s}$ for split to occur, meaning that even a high-speed camera running at 10^6 frames per second (fps) cannot resolve the splitting process.

Figure 2.7 shows the damaging effects of chaotically oscillating bubbles on the microwall arrays. The shapes of the bubble change drastically in each frame that is taken every $100 \text{ }\mu\text{s}$, demonstrating the chaotic and vigorous nature of this type of oscillation. We clearly see that the sections of microwalls indicated by arrows in the figure become dark after being broken by the bubble. However, the extremely fast and unpredictable bubble behavior imaged by the high-speed camera running only at $10\,000$ f.p.s. makes it difficult to gain physical insight into how the chaotically oscillating bubble generates forces strong enough to break microstructures. Hence, we use an array of microcantilevers to measure the forces in the following.

2.4.2 Array of microcantilevers

To measure the forces generated by oscillating bubbles quantitatively, we use an array of silicon microcantilevers as shown in figure 3.1(c), which are deflected by oscillating bubbles as illustrated in figure 2.8(a). We first confirmed that the deflection of the cantilevers due to acoustic streaming and pressure fluctuations in the ultrasonic field is negligible by measuring the deflections in the absence of adjacent bubbles. The resonance frequency of a silicon cantilever of $[w, l, b] = [15, 130, 3] \text{ }\mu\text{m}$ in vacuum, $f_0 = b(E/\rho_c)^{1/2}/(4\pi l^2) = 117 \text{ kHz}$, and that in water, $f_w = f_0[1 + \pi\rho_w/(4\rho_c b)]^{-1/2} = 70 \text{ kHz}$ (Sader, 1998), thus the resonance frequencies are far from the external ultrasonic frequency. Here $E = 160 \text{ GPa}$ and $\rho_c = 2330 \text{ kg m}^{-3}$ are Young's modulus and the density of the cantilever, respectively. We note that the cantilevers situated near the oscillating bubble may influence the motions and forces of the bubble, and the bubble

2.4 Observations of micropattern-damaging processes

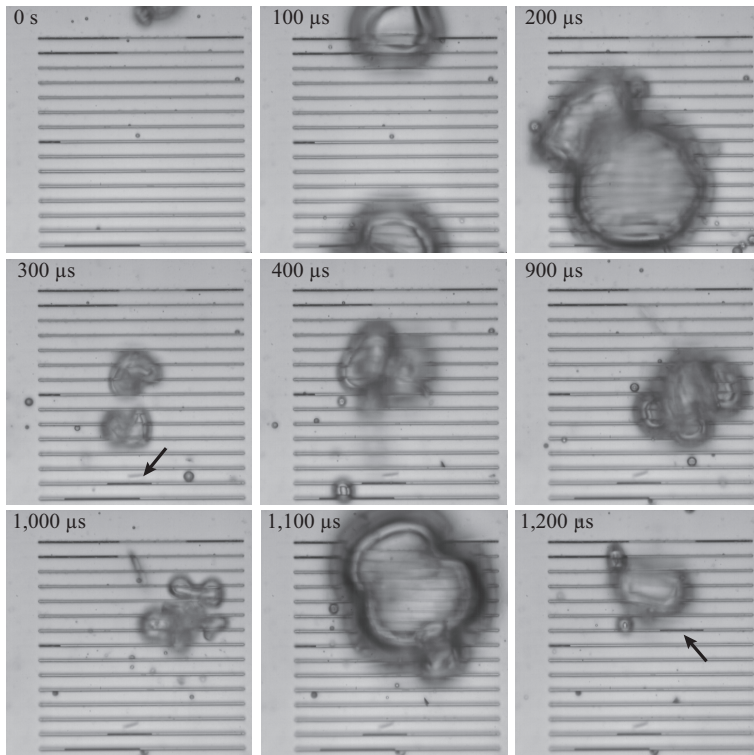


Figure 2.7: Destruction of microwalls due to chaotically oscillating bubbles at $\hat{P} = 63$. The arrows indicate the regions where destruction has occurred.

2.4 Observations of micropattern-damaging processes

motion may in turn affect the cantilever vibration. Such coupling may yield differences in bubble forces compared to those estimated in §2.4.1. However, its effects are expected to be weak because of the significant difference between f_w and the ultrasonic frequency and the relatively small beam width (15 μm) compared to bubble size. When shape and chaotic oscillations arise, the bubble diameter is significantly larger than the beam length as shown in figures 2.8(b) and (d), further reducing the effects of the coupling.

Assuming that the cantilever is subjected to uniform pressure P arising from the bubble oscillation, the maximum displacement occurring at the free end is given by $\delta_m = 3Pl^4/(2Eb^3)$. The characteristic pressure P corresponds to the bubble pressure in figures 2.8(b,d), and to a representative pressure taking into account the bubble pressure exerted over 73% of the cantilever beam length from the anchor and the pressure due to liquid flow over the remaining part of the beam near the free end in figure 2.8(c). We find large differences in δ_m depending on the bubble oscillation mode even at the same acoustic pressure amplitude: different modes are selected by different bubble sizes. Table 3.1 lists the measurement results of δ_m and the corresponding pressure P for each oscillation mode. In the table, δ_m for the shape oscillation and splitting modes corresponds to the maximum deflection observed, and that for the chaotic oscillation is the maximum deflection imaged before destruction.

The shape oscillation as shown in figure 2.8(b) is measured to exert the weakest pressure of the three oscillation modes, 26 kPa, on the cantilever. Taking the characteristic oscillation velocity of the bubble interface, $U \sim \varepsilon\omega R_a \sim \varepsilon\omega R_r \hat{R}$, the characteristic magnitude of dynamic pressure associated with the periodic oscillation of a bubble is scaled as $P_d \sim \rho U^2 \sim \rho \varepsilon^2 \omega^2 R_r^2 \hat{R}^2$. For shape oscillations, $\varepsilon \sim 10^{-1}$, leading to $U \sim 1 \text{ m s}^{-1}$ and $P_d \sim 10 \text{ kPa}$, which is consistent with the measurement results in Table 3.1. Assuming that the pressure of the shape oscillation,

2.4 Observations of micropattern-damaging processes

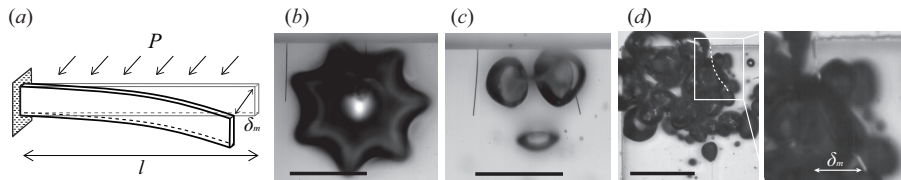


Figure 2.8: Deflection of microcantilevers due to ultrasonic bubbles at $P_a = 76$ kPa. (a) Schematic model. (b) Shape oscillation. (c) Splitting. (d) Chaotic oscillation. The white dashed line has been drawn to aid identification of the microcantilever. Scale bars, $200 \mu\text{m}$

Type	δ_m (μm)	P (kPa)	v_d (m s^{-1})	v_h (m s^{-1})
Shape oscillation	2.6	26	5.1	0.02
Splitting	30.5	308	17.5	0.22
Chaotic oscillation	57.0	575	24.0	0.40

Table 2.1: Measurement results of the deflection of the free end of cantilevers, δ_m , and the corresponding bubble pressure P in each oscillation mode at the constant acoustic pressure condition of $\hat{P} = 63$. We also list the characteristic velocities of liquid flows, v_d and v_h , assuming that the deflection is due to dynamic pressure and water hammer, respectively: $v_d = (P/\rho)^{1/2}$ and $v_h = P/\rho c$.

2.4 Observations of micropattern-damaging processes

$P = 26$ kPa, is due to water hammer, the liquid velocity is estimated to be 0.02 m s^{-1} , which is too low compared to our experimental observations and unlikely to lead to water hammering. If we take $\hat{R} \approx 0.5$ and $\varepsilon \approx 1$ for the splitting mode, and $\hat{R} \approx 1$ and $\varepsilon \approx 1$ for the chaotic oscillation mode, then the dynamic pressure for both modes is scaled as $P_d \sim 10^2$ kPa, in agreement with the experimental values in Table 1. On the other hand, the liquid velocities assuming the water hammer effect, $v_h = 0.22$ and 0.40 m s^{-1} for splitting and chaotic oscillation, respectively, are too low to yield significant water hammer effects. Therefore, the measured pressure values in Table 3.1 correspond to the strength of the dynamic pressure effect not water hammer.

The bubble pressure that can cause the stress at the clamped end of the cantilever to reach the ultimate strength of an etched single crystalline silicon (~ 1 GPa), $P \sim \sigma_u b^2 / (3l^2)$ (Timoshenko & Goodier, 1970), is estimated to be $\sim 10^2$ kPa, a value comparable to the pressure of splitting and chaotically oscillating bubbles in Table 1. We indeed see that microcantilevers are broken by extremely violent motions of chaotically oscillating bubbles in figure 2.9. Although dynamic pressure arising from the chaotic oscillation of a bubble, of the order of 10^2 kPa, is strong enough to break the microcantilever, it is still lower than the pressure needed to break the microwalls ($\sim 10^2$ MPa). This estimate again confirms that the shock effects should come into play to damage the microwalls. Just as a small bubble splitting into two can generate shocks as discussed in §4.1, splitting of multiple bubbles, a typical process in chaotic oscillation, can emit shock waves. Also, secondary shocks due to interaction of the shock and a cloud of bubble can contribute to microstructure damages (Brujan *et al.*, 2011). These high-speed processes leading to emission of shocks that eventually break microstructures like the walls in figure 2.7 cannot be resolved with the present high-speed camera. The shock waves from a cloud of bubbles were captured using a shadowgraph method by Brujan *et al.* (2011).

2.4 Observations of micropattern-damaging processes

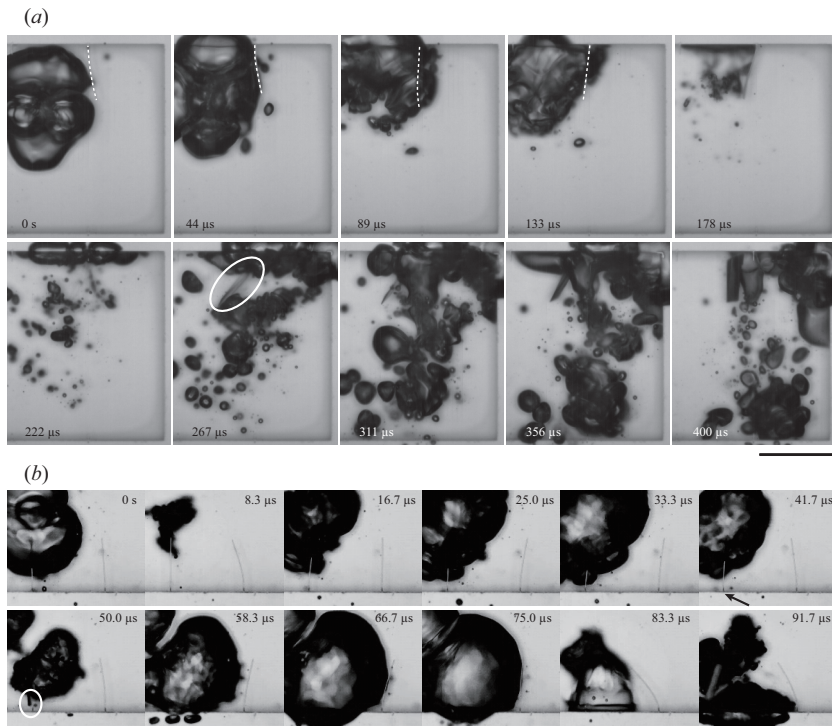


Figure 2.9: High-speed images of a chaotically oscillating bubble breaking a silicon microcantilever. (a) The chaotic oscillation can be extremely violent to lead to the cantilever fracture. The white dashed lines have been drawn to aid identification of the microcantilever. A fragment is shown at $267 \mu\text{s}$ as enclosed by an ellipse. (b) The microcantilever indicated by an arrow disappears between the images of $41.7 \mu\text{s}$ and $50.0 \mu\text{s}$. The fragment is shown at $50.0 \mu\text{s}$ as enclosed by an ellipse. Scale bars, $200 \mu\text{m}$.

We have shown that while microwalls can be broken only by the shock effects of bubble splitting and chaotic oscillation, microcantilevers can be damaged by the dynamic-pressure effects of violently oscillating bubbles. Since the aspect ratio of nanopatterns of integrated-circuit chips steadily increases with the ever-shrinking thickness of the patterns in the current semiconductor manufacturing technology (Wu *et al.*, 2010), the possibility that the dynamic-pressure effects of splitting and chaotically oscillating bubbles may damage nanopatterns grows. Here we estimate the critical aspect ratio of cylindrical pillars, frequently used for nanoelectronic devices including supercapacitors (Chang *et al.*, 2010) and solar cells (Garnett & Yang, 2010), which can be broken by dynamic-pressure effects. The maximum stress occurring at the clamped end under the uniform loading of pressure P is given by $\sigma_m = (16/\pi)(h/a)^2P$ (Timoshenko & Goodier, 1970), where a is the pillar diameter. Figure 2.10 plots σ_m versus the aspect ratio h/a assuming that P is in the range 100 and 900 kPa. It shows that high-aspect-ratio nanopillars adopted in current nanoelectronic chips with h/a exceeding 20 (Henry *et al.*, 2009) can be damaged by the dynamic-pressure effects of violently oscillating microbubbles.

2.5 Conclusions

In summary, we have constructed a regime map of bubble behavior under ultrasonic vibrations identifying the parameter ranges that result in the four distinct oscillation types: volume oscillation, shape oscillation, splitting and chaotic oscillation. Also, we have captured the dynamic processes of microstructure damage due to ultrasonic bubbles, which have rarely been available so far. Our experimental results indicate that liquid jets following the asymmetric collapse of a bubble near a solid wall, which have been frequently assumed to be responsible for solid damage based on the observations made with impulsively generated bubbles, have negligible effects on the microstructures in an ultrasonic field. Rather, damage of microwalls

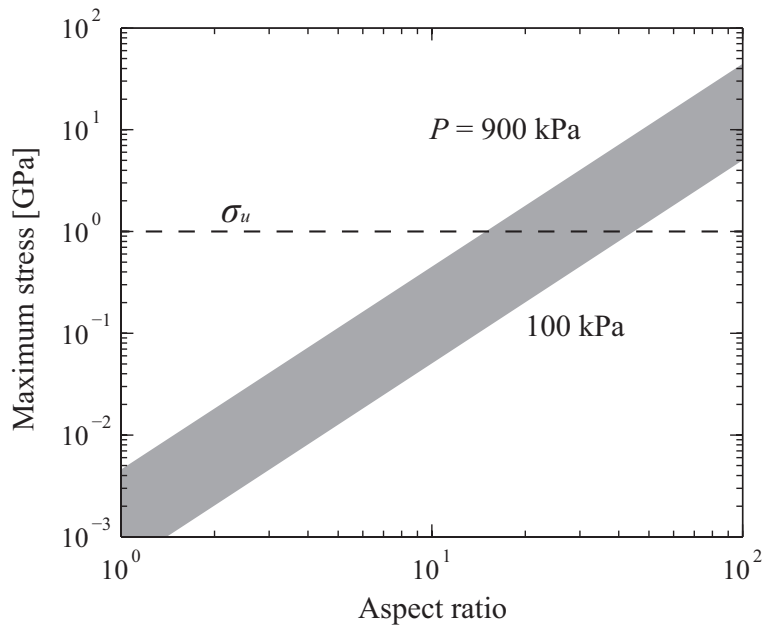


Figure 2.10: Maximum stress at the clamped end of a cylindrical Si pillar due to the uniform pressure P exerted by microbubbles as a function of the aspect ratio, h/a .

2.5 Conclusions

and microcantilevers has been found to occur due to either small bubbles undergoing splitting or large bubbles exhibiting chaotic oscillations. In particular, we have shown that dynamic pressure exerted by violently oscillating bubbles is capable of damaging high-aspect-ratio structures like cantilevers and pillars. To enable the application of the ultrasonic cleaning process in manufacturing of semiconductor chips with extremely fragile nanopatterns of ever-shrinking sizes, the ultrasonic frequency and amplitude should be carefully tuned to minimize the splitting and chaotic oscillation of microbubbles.

This work could be a starting point for a complete understanding of the disruptive behavior of microbubbles in an ultrasonic field, although we have to wait until the high-speed imaging technique catches up with the bubble oscillation speed to acquire detailed, time-resolved information of a violent bubble motion. In addition, our experimental findings can help one to extend the applications of vigorous bubble oscillations to cleaning of membranes (Chen *et al.*, 2006; Lamminen *et al.*, 2004) and even clothes (Gallego-Juarez *et al.*, 2010). Surface modification of metal surfaces for wettability control can also benefit from vigorous bubble oscillations that selectively damage the surface and lead to tailored surface roughness (Belova *et al.*, 2011).

Chapter 3

Visualization and minimization of clustering of microstructures due to liquid film evaporation

3.1 Introduction

When a nanopattern array is immersed in a liquid that is then evaporated, capillary forces associated with the liquid/gas menisci, between free ends of the soft materials, may lead them to deform laterally and adhere to each other. The effect of elastocapillary coalescence (Cohen & Mahadevan, 2003; Kim & Mahadevan, 2006), i.e. the interaction between elastic structures and capillary forces, has long been observed in nature but has just begun to find applications in artificial systems. In elastocapillarity, capillary force plays a crucial role in a wide range of natural phenomena. For example, self-assembly by using capillary force-induced cohesion is useful to fabricate complex hierarchical structures (Duan & Berggren, 2010; Fusi *et al.*, 2011; Pokroy *et al.*, 2009a). However, pattern collapse is a serious problem in the fabrication of fine patterns. As the dimensions of mi-

crostructures decrease and their aspect ratios (defined as the ratio of height to lateral feature size) and pattern densities (defined as the ratio of the pattern area to the unit cell area) increase, the surface area to volume ratio also increases significantly. These high-aspect-ratio microstructures become increasingly susceptible to surface forces and liquid capillary forces, when immersed and dried from a liquid, leading to pattern collapse. Pattern damage has been found to occur during the spin-drying step in semiconductor manufacturing processes. Spin-drying, in which a rinsing liquid deposited on a wafer is rapidly dried by wafer spinning, is an essential step in semiconductor manufacturing processes. As the liquid evaporates, its meniscus straddles neighboring submicron-size patterns. The capillary effects that pull the patterns together could possibly lead to a pattern collapse, when two or more patterns coming in direct contact with each other. Pattern collapses are becoming a serious problem as pattern sizes shrink and aspect ratios increase. It is particularly relevant to the fabrication of high-aspect-ratio structures in semiconductor manufacturing (Fusi *et al.*, 2011; Kim *et al.*, 2012; Tanaka *et al.*, 1993) because it is responsible for the stiction of patterns in rinsing and drying process. Although it was reported that patterns were stuck together due to evaporating liquid, a detailed sequence of pattern collapse has not yet been observed.

The aim of this work was to visualize the dynamic interaction between a pattern and an evaporating liquid, and to develop a model of pattern collapse taking adhesion into account. The simple model, balancing surface adhesive energies and elastic restoring energies, was developed to construct a regime map that guides us to find a process condition that avoids pattern collapse, and was then compared to experimental results. To this end, we experimentally found a critical role of the substrate temperature in preventing the collapse of patterns by changing the evaporation rate and behavior of the liquid film.

3.2 Experiments

In this work, we used an apparatus, as shown in Figure 3.1(a), to observe the interaction between an evaporating film and microstructures during the drying process. We conducted deformation experiments of microscale arrays fabricated in soft elastomeric polymers to mimic nanoscale structures in MEMS devices because it is difficult to visualize the dynamic interaction of high-aspect-ratio nanopatterns and liquid films with an optical instrument. As will be shown, the equivalent moment ratios between micro- and nano- patterns depend on the parameters of the geometry and material's stiffness. The moment ratio in the analysis of pattern collapse is discussed in details in §3.3. The microstructures, fabricated by mixing PDMS (polydimethyl-siloxane; Sylgard 184, Dow-Corning) prepolymer base and the curing agent in a 10:1 ratio (by weight), were poured onto negative patterned silicon masters (fabricated by deep reactive ion etching and treated with an antisticking agent (octafluorocyclobutane, C_4F_8)), and degassed under vacuum for 1 hour to eliminate all air bubbles. Curing was then achieved at 80°C for 1 hour in a conventional oven. The PDMS arrays were carefully peeled off from the silicon master and used without any further surface treatment. As shown in Figure 3.1(b, c), two different shapes of PDMS arrays were fabricated, a cylindrical pillar array and a rectangular array. The width (or diameter) w of the arrays was $\approx 10\ \mu\text{m}$, the spacing d between two adjacent patterns was $\approx 10\ \mu\text{m}$, length l of the rectangular array was $\approx 50\ \mu\text{m}$, and the heights H ranged from 20 to $40\ \mu\text{m}$, respectively. The aspect ratio AR was between 2 and 4. The packing geometry was square ($m \times n$). The resulting pattern density was ≈ 0.196 for the cylindrical pillar array and ≈ 0.250 for the rectangular array. The prepared PDMS patterns were horizontally placed and IPA (isopropyl alcohol, Sigma-Aldrich), which is widely used for wafer cleaning, or HFE-7100 (methoxy-nonafluorobutane, 3M Novec) were injected on the substrate with a syringe. The surface tension coefficients of the rinse liquids

3.3 The process of pattern collapse

Table 3.1: Properties of rinse liquids; surface tension at 25°C, contact angle on a flat PDMS sample, and normal boiling point. *a*, taken from Product information sheet from 3M.

Liquid	Surface tension (mN m ⁻¹)	Contact angle (deg)	Boiling point (°C)
IPA	22.4	22	82.5
HFE-7100 ^a	13.6	< 5	61

are significantly lower than that of water. The contact angles (θ) of the rinse liquids on a PDMS surface were measured by the sessile drop method immediately after deposition, due to their volatility. The rinse liquid properties are summarized in Table 3.1. After fully wetting, the liquid was dried off by natural convection at the ambient conditions (temperature, $\sim 25^\circ\text{C}$; humidity, 30–40%). We used two arrangements for the high-speed camera (Photron SA1.1) to capture the interaction between the patterns and the rinse liquids: a horizontal arrangement for a side view of the pattern with a long distance lens, and a vertical arrangement for a top view with an upright microscope (Olympus BX-51M) and 20–50 \times objective. The two arrangements did not synchronize since the side view of the $m \times n$ array prevented the possibility of quality images of the meniscus behavior from the back of the array, and to remedy this we fabricated one row ($1 \times n$) of the rectangular array for a side view.

3.3 The process of pattern collapse

Figure 3.2(*a–c*) shows the sequence of pattern collapse caused by the liquid film evaporation at each pattern. As shown in Figure 3.2(*a*), the cylindrical pillars are bundled together to form a cluster while dry channels, which are originated from asymmetric capillary force by random facts (Duan & Berggren, 2010), propagate through the entire area. When the

3.3 The process of pattern collapse

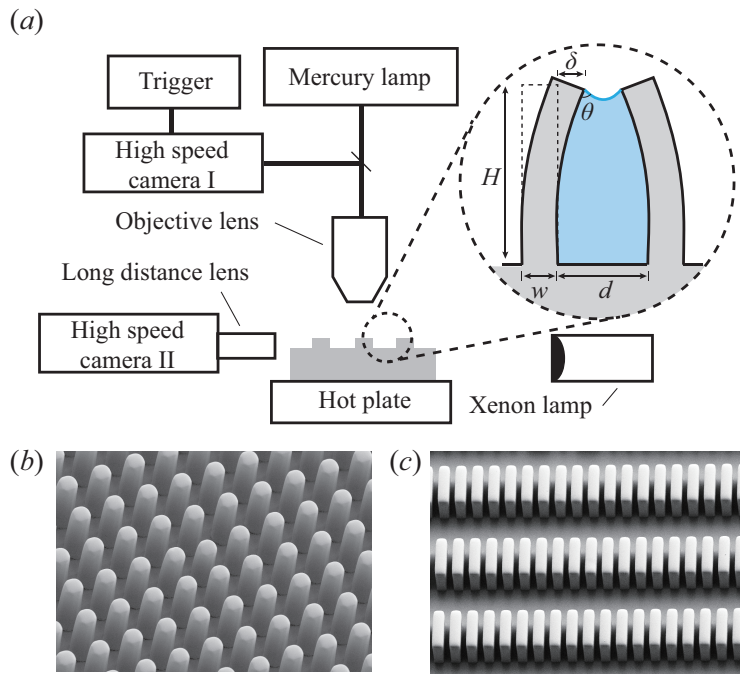


Figure 3.1: (a) Experimental apparatus to image the liquid film behavior in the process of pattern collapse. The upper right inset depicts the interaction of the liquid film and the pattern. (b) Cylindrical pillar array and (c) rectangular array. Scale bars, $50 \mu\text{m}$.

3.3 The process of pattern collapse

liquid evaporates to the level of the free tips, a meniscus connecting neighboring pillars is formed. Imperfections and instabilities, which include local differences in the evaporation rate, pinning of the contact line, and variations in the spacing, will nucleate the first pillar cluster at a particular location. As a result, the next pillar will sense an anisotropic force field and will bend. This process will propagate through the pillars and generating a long-range ordered area where the liquid was wetted on. Figure 3.2(b) shows distortion of the rectangular pattern due to an isolated liquid bridge formed between patterns. In particular, Figure 3.2(c) describes liquid meniscus behavior between patterns in detail. In the initial stages, the menisci are caught at the top of the patterns (the first frame). Subsequently, the surface tension force acts on the three-phase line and pulls the patterns asymmetrically. Also, inherent nonuniformity of the pattern spacing (Pokroy *et al.*, 2009b), or small film disturbances, induces nonuniform evaporation rates of films between the patterns. The symmetry of the meniscus heights or gap widths is broken, as shown in the second frames. The forces of surface tension, which would be balanced if symmetry were maintained, now pull the patterns asymmetrically. The difference of the gap widths gets larger, and this in turn aggravates nonuniformity of evaporation rates. Thus, the liquid height gets progressively more nonuniform as shown in the third and fourth frames, and a negative Laplace pressure is exerted on the pattern's side wall. Therefore, the patterns contact each other by surface tension and strongly adhere together due to the negative Laplace pressure. As evaporation continues, the lower meniscus rises up as shown in fifth frame because the evaporation rate, which is proportional to the area, is faster there. Finally, the patterns are stuck together after the liquid film disappears at the tip of the patterns, as shown in last frames, and permanent adhesion of the patterns arise due to surface adhesive forces (short-range van der Waals interactions or solid surface energies) (Kendall, 1994). After complete evaporation of the liquid, the state of the patterns,

3.3 The process of pattern collapse

whether freestanding or collapsed, was checked with the optical microscope and the scanning electron microscopy (SEM) images as shown in Figure 3.2(*d, e*). As can be observed, there were no plastic deformations.

Previous studies of pattern collapse reported that the rinsing liquid, and its related capillary forces, were considered only in the context of the Laplace pressure (Cao *et al.*, 2000; Duan & Berggren, 2010; Jincao *et al.*, 2001; Tanaka *et al.*, 1993). For cases when the patterns are completely surrounded by liquid, a lateral capillary meniscus interaction force also acts on the patterns (Chandra & Yang, 2009). However, after complete evaporation of the liquid film, capillary forces are no longer exerted on the patterns. The final equilibrium state of patterns adhered to each other permanently has not yet been considered. Therefore, we describe the dynamic interaction of the pattern and evaporating film due to capillary forces, and then analyze the final state by comparing the adhesion energy and elastic resistance energy of the patterns

3.3.1 End-contact due to capillary forces during evaporation

As shown in Figure 3.2, capillary forces are composed of the Laplace pressure and surface tension force. Pattern collapse may be related to the forces associated with the liquid/air menisci at the free ends, which lead to a moment or torque acting on the patterns. To evaluate the probability of pattern collapse, we compared the bending moment and the elastic resistance to bending. Details of the configuration for two dimensions can be seen in the upper right inset of Figure 3.1(*a*). This is the severest condition for pattern collapse. The bending moment (M_b) at the clamped end is expressed as (Chandra & Yang, 2009)

$$M_b \sim \sigma H \sin \theta + \frac{\sigma H^2 \cos \theta}{d} \quad (3.1)$$

where σ is the surface tension coefficient between the drying liquid and air, H is the pattern height, d is the spacing, and θ is the equilibrium contact

3.3 The process of pattern collapse

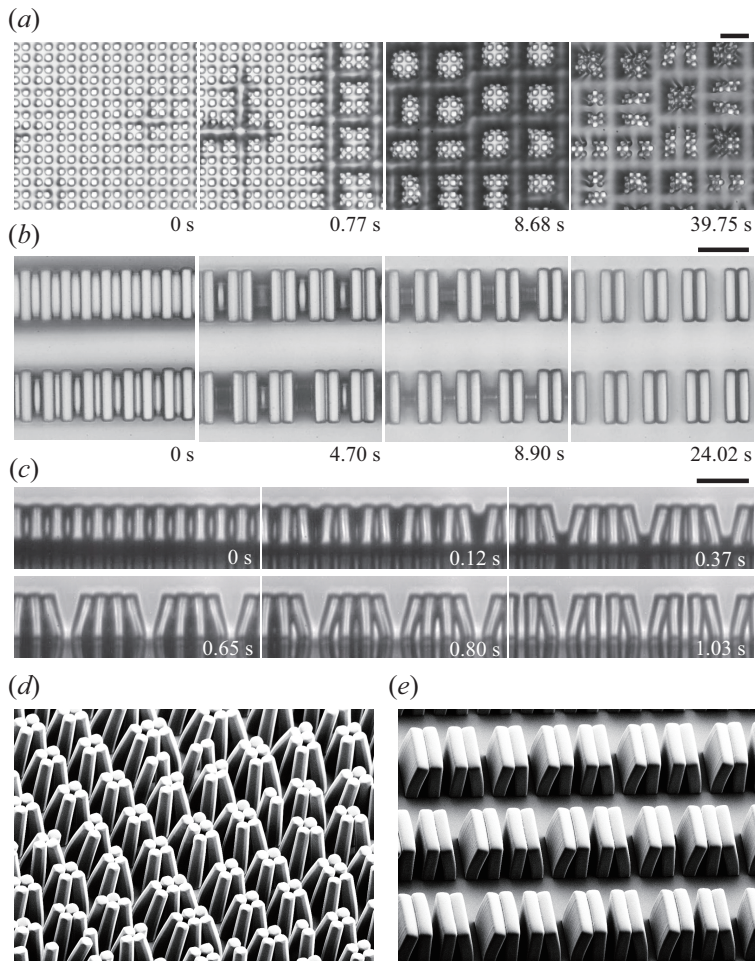


Figure 3.2: The process of pattern collapse. Samples with $AR = 4$ were rinsed by IPA, and then dried at room condition. (a) Top view of cylindrical pillar array and (b) $m \times n$ rectangular array. (c) Side view of $1 \times n$ rectangular array. (d) Scanning-electron microscopy (SEM) images of collapsed pillar array and (e) rectangular array. Scale bars, 50 μm .

3.3 The process of pattern collapse

angle of the drying liquid with the pattern surface. In this equation, the first term is due to surface tension which is a concentrated force operating on the three-phase line (Chini & Amirfazli, 2010), and the second term is a result of negative pressure by liquid height differences. The pressure inside the liquid is different from the pressure of the surroundings due to the pressure jump across the interface, which is referred to as the Laplace pressure. When the solid is wettable, the interior pressure is lower than that of the surroundings, leading to negative (relative) pressure. The elastic resistance moment (M_r) acting on the deflected pattern is scaled by using an elastic beam bending model supported at one end (Timoshenko & Goodier, 1970) which excludes plastic deformation, poor adhesion to the substrate (peeling), and swelling probability.

$$M_r \sim \frac{EI\delta}{H^2} \quad (3.2)$$

where E is the Young's modulus of the structure (≈ 1.7 MPa for PDMS), I is the area moment of inertia ($I = w^3/12$ for 2D rectangular shape), and δ is the maximum displacement at the free end. The relative magnitudes of the bending moment and the resistance moment determine whether patterns get stuck together. When the maximum displacement is half the spacing, $\delta = d/2$, the moment ratio is $M_b/M_r \sim 24\sigma(H/w)^4[(w/H)\sin\theta + (w/d)\cos\theta]/Ed$. For high-aspect-ratio structures, $AR = H/w \gg 1$, the moment ratio can be reduced by

$$\frac{M_b}{M_r} \sim 24 \frac{w\sigma \cos\theta}{Ed^2} (AR)^4 \quad (3.3)$$

However, if H and w are of the same order, then the surface tension term, $\sim \sigma \sin\theta$, cannot be negligible. Consider the case of the cylindrical pillar array which has a circular cross-section, $I = \pi w^4/64$. During the liquid evaporation, capillary forces pull the multiple pillars towards the center of aggregate as shown in Figure 3.2(a). The pillars bend toward the diagonal direction, $\delta = \sqrt{2}d/2$. Therefore, the moment ratio of the cylindrical pillar can be

3.3 The process of pattern collapse

expressed by $M_b/M_r \sim 64\sqrt{2}\sigma(H/w)^4[(w/H)\sin\theta + \sqrt{2}(w/d)\cos\theta]/\pi Ed$. For high-aspect-ratio pillars, the moment ratio reduces to

$$\frac{M_b}{M_r} \sim \frac{128}{\pi} \frac{w\sigma \cos\theta}{Ed^2} (AR)^4 \quad (3.4)$$

Since the moment ratio of a pillar array is larger than that of a rectangular array, multiple pillars stick together compared to the rectangular array where two patterns stick together during liquid evaporation, as shown in Figure 3.2(a) and (b). The equations (3.3, 3.4) reveal that patterns with high aspect ratios, narrow spacing, and softer materials more readily stick together when surrounded by high surface-tension liquids (as AR increases, and as d and E decrease, the moment ratio increases). In particular, the aspect ratio of the pattern plays a dominant role causing pattern collapse during a rinse-dry, as the moment ratio is proportional to the fourth power of AR .

Figure 3.3(a) shows how the moment ratio varies with AR for our experimental data and previous studies. Since previous efforts have mainly focused on the results before and after the rinse liquid drying process, without investigating the process of pattern collapse, the intermediate process, which shows interaction by capillary force, has not been seen. We assume permanent adhesion of the patterns in previous results, as they are in contact at their tips they will stay in their adhered state once capillary force bring them together. However, several results in Figure 3.3(a) cannot explain the direct contact of the patterns. In particular, in the experimental result of $M_b/M_r > \sim 1$ (half-filled symbols), the bent microstructures return to their upright position once the liquid evaporated as shown in Figure 3.3(b). This is observed not only by the capillary force generated during evaporation of the liquid film, but also by the energy balances of the final state of patterns.

3.3 The process of pattern collapse

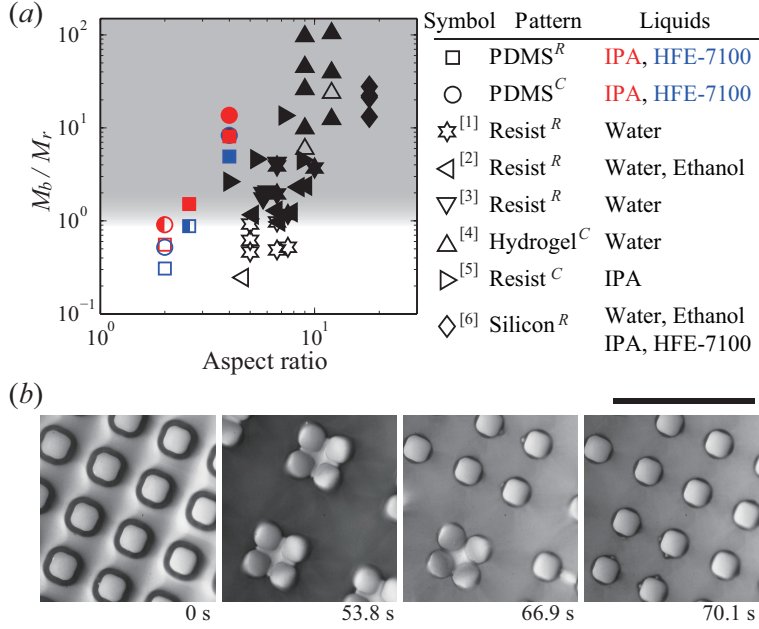


Figure 3.3: (a) Contact regime map : the moment ratio as a function of aspect ratio. Experimentally the patterns were collapsed in the gray regime. The superscript *R*, rectangular array; *C*, cylindrical pillar array. The half-filled symbol correspond to recovered pattern after contact each other. Previous experimental data: [1], Deguchi *et al.* (1992); [2], Tanaka *et al.* (1993); [3], Tanaka *et al.* (1994b); [4], Chandra & Yang (2010); [5], Duan & Berggren (2010); [6], Kim *et al.* (2012). (b) Top view of cylindrical pillar array with $AR = 2$ was rinsed by IPA, and that was recovered after contact. Scale bar, $50 \mu\text{m}$.

3.3 The process of pattern collapse

3.3.2 Permanent adhesion due to surface energy after evaporation

As evaporation continues, the liquid film disappears at the tip of the pattern. At this stage, capillary forces are no longer present. As a consequence, a large fraction of the deformation energy stored in the bent columns, bring them back to their original shape, as the tensile stresses due to capillary forces are absent after evaporation. Thus adhesion arises due to the solid surface energy (γ_s , energy per unit area). The stability of the final states of the pattern depends on the competition between the elastic strain energy of the pattern and the adhesive energy between patterns. As the stiffness of the pillars decreases, adhesive energy begins to dominate, leading to permanent adhesion (Chandra *et al.*, 2008). The problem is analogous to the lateral collapse in microcontact printing or replica molding of soft-lithography techniques (Hui *et al.*, 2002; Lee *et al.*, 2005; Zhang *et al.*, 2006). According to the Dupré equation, the work of adhesion (W), which is the reversible work required to pull apart a unit area of the interface, can be expressed in terms of surface energy, $W \sim 2\gamma_s$. After separation, each equal surface has a surface energy γ_s which can pull the surfaces back into contact (Kendall, 1994). The surface energies of materials are summarized in Table 3.2. We used the definition of the adhesive energy, W_{ad} , which is W multiplied by the area of contact.

We analyzed the permanent adhesion in terms of competition between the work of adhesion due to surface energy and the elastic strain energy of the patterns. In order to compare the relative magnitude of changing in elastic energy and changing in adhesive energy, we performed a scaling model following the approach used by Hui *et al.* (2000) and Glassmaker *et al.* (2004) Consider the situation, depicted in Figure 3.4(a), where two rectangular patterns adhere to each other. Let h be the height of the noncontact region. All the elastic strain energy is stored in the region where elastic bending deformation is dominant. The total strain en-

3.3 The process of pattern collapse

Table 3.2: Surface energy in air and Young’s modulus of materials: a , taken from Chaudhury & Whitesides (1991); b , taken from Bauer *et al.* (1996); c , taken from Chandra & Yang (2010); d , the surface energy of bare silicon is much higher (1400 mJ m⁻²). We used a silicon substrate with a thick oxide layer taken from Yu *et al.* (2001).

Material	Surface energy (mJ m ⁻²)	Young’s modulus (MPa)
PDMS	22 ^a	10 ⁰
Resist	~50 ^b	10 ³
Hydrogel	33 ^c	10 ¹ –10 ³
Silicon	~115 ^d	10 ⁵

ergy is scaled as $E_{el} \sim M^2h/EI$ and it is proportional to the square of the bending moment. By using equation (3.2), the total strain energy is expressed as $E_{el} \sim EId^2/4h^3$. As h increases, the elastic strain energy decreases, and one can calculate the decrease in strain energy resulting from a differential increase Δh in the height of the noncontact region as, $-\Delta E_{el}/\Delta h \sim 3EId^2/4h^4$. In equilibrium, the energy changes equals work ΔW_{ad} needed to decrease the contact area by Δh . The change in work of adhesion is given by, $\Delta W_{ad}/\Delta h \sim 2\gamma_s l_c$, where l_c is a contact length of the rectangular pattern. The energy ratio of the work of adhesion to the elastic strain energy is given by

$$\frac{\Delta W_{ad}}{\Delta E_{el}} \sim 32 \frac{w\gamma_s}{Ed^2} \left(\frac{l_c}{l} \right) (AR)^4 \quad (3.5)$$

This equation implies that patterns with a high-aspect-ratio or made of soft material with higher surface energy are easier to adhere. To obtain the final state for pattern collapse, only elasticity and adhesion were considered. For the cylindrical pillar array as shown in Figure 3.4(b), the situation for pillars is somewhat altered. When four identical cylinders are placed in closed proximity, the surfaces will cause the cylinders to jump into contact

3.3 The process of pattern collapse

and adhere. Once two neighboring pillars make contact, the contact area increases, owing to the action of the surface energy near the edge of the contact. The equilibrium contact width (w_c) of two identical circular cylinders can be determined using the JKR theory (Hui *et al.*, 2000; Johnson *et al.*, 1971), $w_c \sim 4(w^2\gamma_s/\pi E)^{1/3}$. Due to deformation near the contact region, there is an accompanying stored elastic energy in the pillars, $E_{st} \sim \gamma_s w_c/2$. Since a pillar is in contact with two neighboring pillars, the pillar has two contact widths as shown in Figure 3.2(d). In equilibrium, decreasing in strain energy is equal to the energy required to separate the four surfaces, i.e. $\Delta W_{ad}/\Delta h \sim 2(2\gamma_s w_c - E_{st}) \sim 3\gamma_s w_c$. The energy ratio of the pillars, which adhered together in a group of four, is

$$\frac{\Delta W_{ad}}{\Delta E_{el}} \sim \frac{128}{\pi} \frac{w\gamma_s}{Ed^2} \left(\frac{w_c}{w}\right) (AR)^4 \quad (3.6)$$

If the work of adhesion between the adhered patterns is larger than the elastic energy acting to restore the patterns to their original shape, the adhesion would be sustained after drying. So, after the complete drying of the pattern, their permanent adhesion is determined by the magnitude of the solid surface energy and elastic restoring energy, which is not related to the capillary forces of the liquid. Figure 3.4(c) shows the energy ratio of pattern for each type. Through the regime map of the energy ratio, we can find the reason of the phenomena, which is not explained in the contact regime map of the Figure 3.3(a). Although the patterns ($M_b/M_r > \sim 1$ and $\Delta W_{ad}/\Delta E_{el} < 1$) are stuck together due to capillary forces, the patterns are restored after drying since the elastic restoring energy is larger than the adhesion energy. According to equations (3.5, 3.6), the aspect ratios of the rectangular array and the pillar array need to be shorter than ≈ 2.2 and ≈ 2.9 , respectively, to avoid any permanent adhesion, once brought into contact. Figure 3.4(c) indicates that experimental results of present work agree well with the theoretical predictions. No pattern collapse was observed when the energy ratios were smaller than unity, with

3.3 The process of pattern collapse

exception of one case: hydrogel pillar with $w = d = 750$ nm, and $AR = 12$, which were predicted to remain collapsed but were found experimentally to be separated. The discrepancy between experiment and theory might be attributed to the swelling nature of hydrogel.

So far, we have observed the detailed sequence of pattern collapse and explained the mechanism. Possible remedies to pattern collapse according to the moment ratio of equations (3.3, 3.4) can be categorized into two groups: (i) increasing either the resistance moment by enhancing stiffness of material (Shibata *et al.*, 1997; Tanaka *et al.*, 1994a) or the spacing between patterns (Cao *et al.*, 2000); (ii) decreasing either the bending moment by approaching the contact angle at the three-phase line to 90° (Kondo *et al.*, 2005) or the surface tension of rinse liquid with liquid CO_2 (Jincao *et al.*, 2001). Since pattern contact due to capillary forces of the rinse liquid is a necessary condition for pattern collapse, the fundamental way to prevent pattern collapse is to eliminate capillary forces via supercritical fluids (Nakatsu *et al.*, 1999). However, supercritical drying processes have problems in several steps that use high pressure. Another viable method to minimize the permanent adhesion is to reduce the energy ratio by decreasing surface energy of the material, enhancing the stiffness, or changing the pattern's geometry. However, to avoid pattern adhesion, there is a need to change other factors such as the evaporating film behavior and substrate temperature, because a pattern's geometry and material are dictated by design requirements and their electrochemical properties. Therefore, we introduce a new solution that maintains reduced adhesion energy by decreasing the contact length (l_c or w_c) of patterns. A rectangular array with $AR = 2.6$ can retain contact as long as it is held together when contacting along the longitudinal direction of the pattern after drying ($\Delta W_{ad}/\Delta E_{el} > 1$). However, the pattern is detached because the work of adhesion is reduced when the contact length is reduced ($l_c/l < 1$), as shown in Figure 3.4(d). The contact area between patterns can be adjusted by changing the evaporation

3.4 The effects of substrate temperature

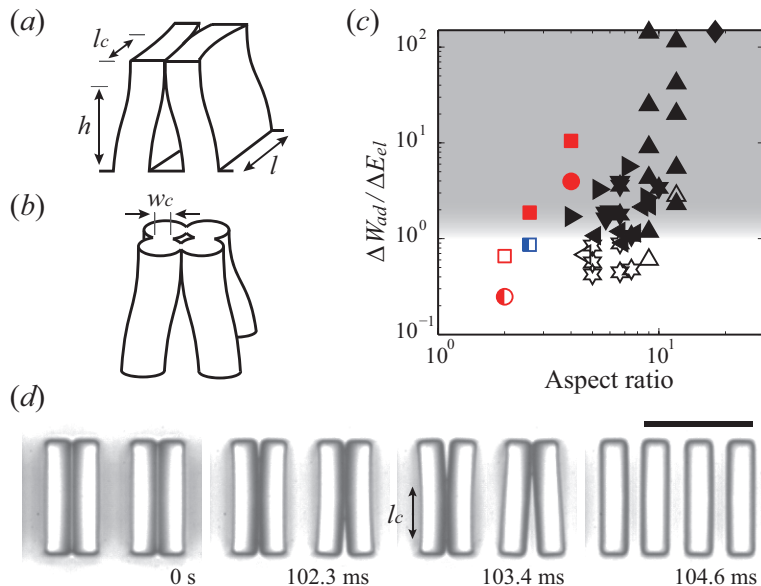


Figure 3.4: Permanent adhesion due to surface energy. (a) Schematic models of a rectangular array and (b) a cylindrical pillar array. (c) Adhesion regime map : the energy ratio as a function of aspect ratio. (d) Top view of rectangular array with $AR = 2.6$. This array was rinsed with HFE-7100, and then restored due to decreasing of contact length ($l_c/l \approx 0.47$). Scale bar, $50 \mu\text{m}$.

film behavior. If the evaporating thin film between patterns were trapped at the top of the patterns, the thin film would prevent direct contact of the patterns, reducing the contact area (we call that “wet contact”).

3.4 The effects of substrate temperature

We focus on preventing direct contact of solid surfaces to maintain a wet contact (thin film between patterns) by controlling temperature. As a possible remedy to maintaining a wet contact, we attempted to change the evaporation behavior by increasing the substrate temperature. In this study, we heated the micropattern surface using a hot plate. Figure 3.5(a, b)

3.4 The effects of substrate temperature

show the patterns were restored on the high temperature substrate. Figure 3.5(c) clearly shows the effects of the heated substrate on meniscus behavior. The liquid disappears at the bottom due to evaporation there, and its bottom meniscus rapidly rises up, decreasing the liquid height difference. The film completely disappears as liquid trapped at the top of the pattern vanishes, at which moment the clustered patterns are separated from each other as shown in Figure 3.5(b).

We have two explanations for why the high temperature substrate leads to minimization of pattern collapse. First, the substrate temperature changes the evaporation rate and behavior of the liquid film. We compare thin film behavior at room temperature and at high temperature. At room temperature, the liquid film also disappears at the bottom and with a rising meniscus, and the thin film is trapped at the top of the patterns (4.70 s). However, the thin film already dries before neighboring liquid films dry and maintain dry contact (8.90 s) as shown in Figure 3.2(c). On the other hand, on the high temperature substrate, the thin film, which is trapped at the top of the patterns until the liquid film arises, prevents direct contact of solid surfaces to maintain wet contact by the rising liquids. Also, the wet contact reduces the surface energy. In other words, a low energy liquid easily reduced the magnitude of the interaction compared to the case in air, freeing each surface to interact directly with the liquid (Delamarche *et al.*, 1997). Chaudhury & Whitesides (1991) have measured that the surface energy of PDMS immersed in methanol, which has a similar surface tension with IPA, $\approx 3 \text{ mJ m}^{-2}$, is about 1 order of magnitude smaller than that of PDMS in air, $\approx 22 \text{ mJ m}^{-2}$ or in water(non-wetting liquid), $\approx 43 \text{ mJ m}^{-2}$, respectively. Thus, the total work of adhesion decreases, and finally patterns are restored as shown in Figure 3.5(a–c). Figure 3.5(d) shows schematic illustration of the pattern restoration by the wet contact. The rapidly decreasing liquid height difference leads to a decreasing of the

3.4 The effects of substrate temperature

negative Laplace pressure. The bending moment is rewritten to take into account the liquid height difference as

$$M_b \sim \sigma H \sin \theta + \frac{\sigma \Delta h_l (2H - \Delta h_l) \cos \theta}{d} \quad (3.7)$$

where Δh_l is the liquid height difference as shown in Figure 3.5(d). As the height difference decreases rapidly, the reduced bending moment may lead to weak adhesion.

Secondly, temperature may lead to a variation in physical properties of the material and liquid. Typically, as temperature of a liquid increases, its coefficient of surface tension decreases. In case of IPA, the coefficient of surface tension $\sigma \approx 15 \text{ mN m}^{-1}$ at the boiling point (Yaws, 1999). Also, there is a linear dependence of the elastic modulus of the PDMS on the temperature, $E \approx 3 \text{ MPa}$ at 180°C (Schneider *et al.*, 2008). However, even though the physical properties depend on temperature, the moment and energy ratios of the patterns on the high temperature substrate still exist in contact and adhesion regimes, i.e. $M_b/M_r \approx 3$ and $\Delta W_{ad}/\Delta E_{el} \approx 6$ for the rectangular array with $AR = 4$, respectively, so that the patterns contact each other due to the capillary force and stay in their adhered state. Therefore, the variation of physical properties plays a minor role in pattern restoration.

Figure 3.5(e,f) plot the experimentally determined pattern-collapse probabilities (a ratio of the number of patterns clustered to the total number of patterns by using top view of the microscopic images) versus substrate temperature. The collapse probability decreases as the pattern temperature increases. Above 100°C , collapse of rectangular arrays was completely prevented for all the micropattern samples tested. However, the cylindrical pillars array still saw collapses since the pillars which collapsed together in groups of more than four needed faster rising rate of the liquid film (or higher substrate temperature) than rectangular patterns to separate them. The evaporation rate may play a role in the drying process. The faster

evaporation rate of HFE-7100 induces dry contact of the patterns although its surface tension coefficient is smaller than that of IPA.

To check whether the wet contact of the pattern indeed plays an important role in pattern recovery, we manipulated dry contact of the patterns by dry air (velocity, $\sim 8 \text{ m s}^{-1}$; temperature, $\sim 70^\circ\text{C}$; humidity, $\sim 2.8\%$). Figure 3.6 illustrates the experimental evidence. The hot dry air induces fast evaporation rates at the upper meniscus. Therefore, the thin film trapped at the top of the pattern was completely dried. The results indicated that dry contact increases the contact area between the patterns and aggravates pattern collapse probabilities. Even partially restored, the patterns were found to be metastable because their adhesive energy was already above the elastic restoring energy. Therefore, any small environmental perturbation due to dry air may easily lead to pattern collapse on a high temperature substrate (Zhang *et al.*, 2006).

3.5 Conclusions

Fine patterns of high aspect ratio easily stick together during the drying process, a situation where the capillary forces due to retained liquid between the patterns are sufficiently large to cause them to contact. Once contact occurs, the contact area increases and the patterns may adhere to each other as a result of surface adhesive forces. We have observed the detailed sequence of pattern collapse due to liquid film evaporation and constructed a regime map that guides us to predict the stability of pattern collapse via balancing the effects of elastic and capillary forces (or adhesive energies). Here, we introduced an experimental method of improving pattern collapse problems by raising the temperature of pattern surfaces, which controls the thin film behavior between patterns. On a high temperature substrate, the meniscus of the liquid rises up and completely disappears as liquid trapped at the top of the patterns vanishes last. Thus, the thin film between patterns prevents direct contact of the patterns and reduces

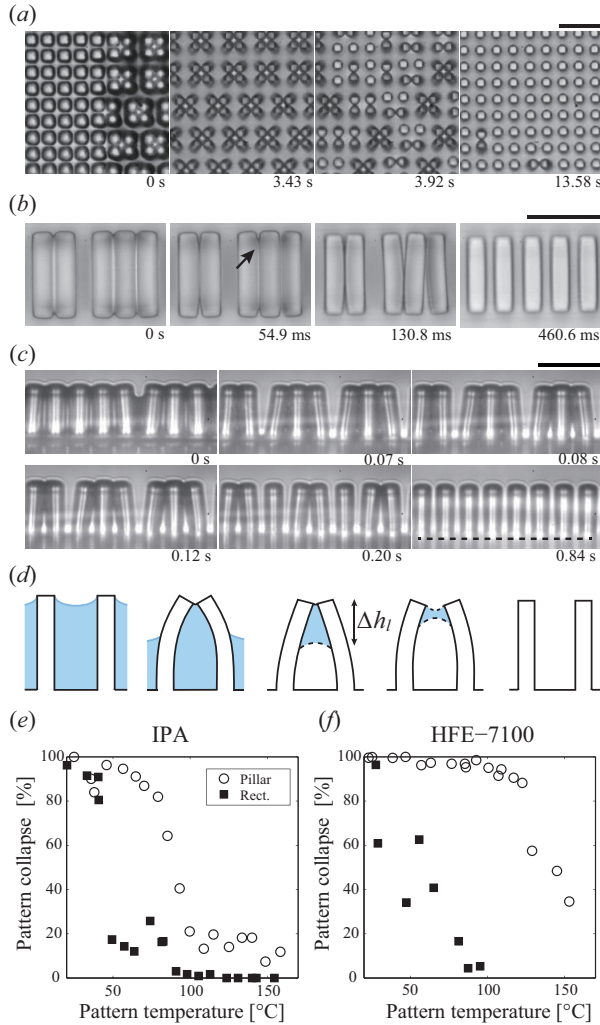


Figure 3.5: Restoration of micro arrays on the high temperature substrate. The samples with $AR = 4$ were rinsed with IPA, and then dried on the high temperature substrate. (a) Top view of a cylindrical pillar array at 149°C and (b) a rectangular array at 146°C. The thin film, indicated by the arrow, trapped at the top of the pattern. (c) Side view of a rectangular array at 184°C. The dashed line has been drawn to aid identification of the substrate. Scale bars, 50 μm . (d) Schematic illustration of pattern restoration. (e) Probabilities of pattern collapse as a function of pattern temperature with IPA and (f) HFE-7100.

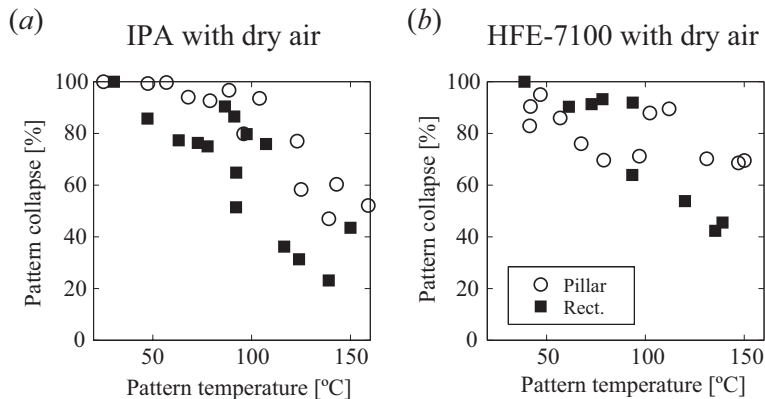


Figure 3.6: Dry contact aggravates pattern collapse probability. (a) Probabilities of pattern collapse with dry air as a function of pattern temperature with IPA and (b) HFE-7100.

in surface adhesive energy. Also, the fast evaporation, which controls the liquid height between patterns, facilitates separation of those.

This work can be a starting point to a complete understanding of the process of pattern collapse due to liquid film evaporation, although we have used microscale structures to visualize it. However, our experimental findings can help one to extend the applications of nanometer-size patterns in semiconductor manufacturing; Kim *et al.* (2013) reported a way to improve the collapse of an order of 30 nm pattern by increasing temperature although they considered only reducing in surface tension.

Chapter 4

Concluding remarks

4.1 Conclusions

In this thesis, we have observed the dynamic interaction between microstructures and liquid interfaces of either bubbles or evaporating films in semiconductor cleaning processes. The experimental results allow us to construct regime maps that can predict the bubble behavior near microstructures in ultrasonic cleaning and the final state of patterns in drying process.

In Chapter 2, we have constructed a regime map of bubble behavior under ultrasonic vibrations identifying the parameter ranges that result in the four distinct oscillation types: volume oscillation, shape oscillation, splitting and chaotic oscillation. Also, we have captured the dynamic processes of microstructure damage due to ultrasonic bubbles, which have rarely been available so far. Our experimental results indicate that liquid jets following the asymmetric collapse of a bubble near a solid wall, which have been frequently assumed to be responsible for solid damages based on the observations made with impulsively generated bubbles, have negligible effects on the microstructures in ultrasonic field. Rather, damages of microwalls and microcantilevers have been found to occur due to either small bubbles undergoing splitting or large bubbles exhibiting chaotic oscillations. In partic-

ular, we have shown that dynamic pressure exerted by violently oscillating bubbles is capable of damaging high-aspect-ratio structures like cantilevers and pillars. To enable the application of the ultrasonic cleaning process in manufacturing of semiconductor chips with extremely fragile nanopatterns of ever-shrinking sizes, the ultrasonic frequency and amplitude should be carefully tuned to minimize the splitting and chaotic oscillation of microbubbles.

In Chapter 3, we have considered the roles of capillary forces and adhesive energies in the adhesion of microstructures. Fine patterns of high aspect ratio are easily stuck together during the drying process, a situation where the capillary forces due to retained liquid between the patterns are sufficiently large to cause them to contact. Once contact occurs, the contact area increases and the patterns may adhere to each other as a result of surface adhesive forces. We have observed the detailed sequence of pattern collapse due to liquid film evaporation and constructed a regime map that guides us to predict the stability of the pattern collapse via balancing the effects of elastic and capillary forces (or adhesive energies). Here, we introduced an experimental method of improving pattern collapse problems by raising the temperature of pattern surfaces, which controls the thin film behavior between patterns. At high temperature substrate, the meniscus of the liquid rises up and completely disappears as liquid trapped at the top of the patterns vanishes. Thus, the thin film between patterns prevents direct contact of the patterns and reduces in surface adhesive energy. Also, the fast evaporation which controls the liquid height between patterns facilitates separation of those.

This study directly observed the pattern damage phenomenon which occur during microstructure cleaning process and contributed to the understanding of the mechanism behind pattern damages. Moreover, based on the observation results, methods of minimizing structural damage were researched. Through this, a firm basis can be established to minimize the

chronic problem of pattern damage, which occurs during the cleaning process of the semiconductor fabrication process fundamental to modern industries and MEMS fabrication process, while enhancing the microstructure production yield rate and guaranteeing reliability of fabrication processes.

4.2 Outlook

The most relevant industrial problem involving interaction of the micro- or nanoscale structure and liquid interfaces is found in semiconductor circuit manufacturing. With a trend of ever-shrinking feature sizes, the widths and gaps of linear patterns on wafers are now well below 100 nm. Those nanostructures as shown in Figure 4.1(a) are essential building blocks for nanoelectronic devices such as capacitors and electrodes in ultra large-scale integrated circuits. In general, the patterned wafers are washed with ultrasonic bubbles, rinsing solutions (see Figure 4.2) and eventually dried, implying that the liquid interfaces are formed by either bubbles near patterns or evaporating liquid films between the patterns with no exceptions in manufacturing. It is known that as the aspect ratio of the patterns increases and the gap between them decreases, the number of distorted patterns as shown in Figure 4.1(b) increases, deteriorating the chip performance and the yield of the chip manufacturing process. In this small scale, the interactions of the adjacent patterns can arise due to the intermolecular forces such as the van der Waals forces and/or the surface forces as well as the capillary forces. We will develop and experimentally verify theoretical models for the deformation and eventual damages of the microscale patterns due to interfacial forces originating from capillarity, van der Waals and/or surface interactions. This will provide a basic guide for the circuit designers so that pattern failures can be prevented in the design stages. Furthermore, we will suggest novel geometric designs and materials for the patterns that

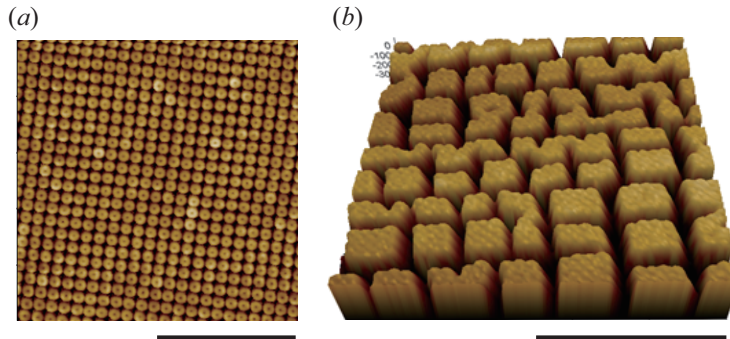


Figure 4.1: Atomic force microscope (AFM) images of a nanopillar array of silicon. (a) Top view of free-standing nanopillar array. (b) Tilted view of distorted nanopillar array. Scale bars, 1 μm .

can endure interfacial forces at higher aspect ratios, which will greatly help the chip manufacturers to enhance the circuit performance and density.

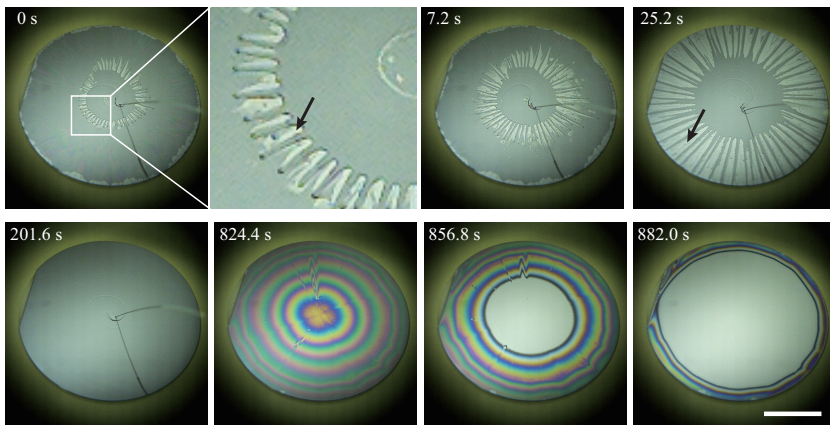


Figure 4.2: IPA rinsing process in spin drying. IPA was injected on the thin film of water. Then the IPA repelled the water films and developed fingering of the IPA. The arrows indicate the dried areas due to IPA repulsion. Scale bar, 5 cm.

References

- BAUER, J., DRESCHER, G. & ILLIG, M. (1996). Surface tension, adhesion and wetting of materials for photolithographic process. *J. Vac. Sci. Technol. B*, **14**, 2485–2492.
- BELOVA, V., GORIN, D.A., SHCHUKIN, D.G. & MOHWALD, H. (2011). Controlled effect of ultrasonic cavitation on hydrophobic/hydrophilic surfaces. *Acs Appl. Mater. Interfaces*, **3**, 417–425.
- BENJAMIN, T.B. & ELLIS, A.T. (1966). The collapse of cavitation bubbles and the pressures thereby produced against solid boundaries. *Phil. Trans. R. Soc. Lond. A*, **260**, 221–240.
- BRUJAN, E., IKEDA, T., YOSHINAKA, K. & MATSUMOTO, Y. (2011). The final stage of the collapse of a cloud of bubbles close to a rigid boundary. *Ultrason. Sonochem.*, **18**, 59–64.
- BRUJAN, E.A., NAHEN, K., SCHMIDT, P. & VOGEL, A. (2001). Dynamics of laser-induced cavitation bubbles near an elastic boundary. *J. Fluid Mech.*, **433**, 251–281.
- BUSNAINA, A.A. & GALE, G.W. (1997). Removal of silica particles from silicon substrates using megasonic cleaning. *Particul. Sci. Technol.*, **15**, 361–369.

REFERENCES

- CAO, H.B., NEALEY, P.F. & DOMKE, W.D. (2000). Comparison of resist collapse properties for deep ultraviolet and 193 nm resist platforms. *J. Vac. Sci. Technol. B*, **18**, 3303–3307.
- CHANDRA, D. & YANG, S. (2009). Capillary-force-induced clustering of micropillar arrays: is it caused by isolated capillary bridges or by the lateral capillary meniscus interaction force? *Langmuir*, **25**, 10430–10434.
- CHANDRA, D. & YANG, S. (2010). Stability of high-aspect-ratio micropillar arrays against adhesive and capillary forces. *Acc. Chem. Res.*, **43**, 1080–1091.
- CHANDRA, D., TAYLOR, J.A. & YANG, S. (2008). Replica molding of high-aspect-ratio (sub-) micron hydrogel pillar arrays and their stability in air and solvents. *Soft Matter*, **4**, 979–984.
- CHANG, S.W., OH, J., BOLES, S.T. & THOMPSON, C.V. (2010). Fabrication of silicon nanopillar-based nanocapacitor arrays. *Appl. Phys. Lett.*, **96**, 153108.
- CHAUDHURY, M.K. & WHITESIDES, G.M. (1991). Direct measurement of interfacial interactions between semispherical lenses and flat sheets of poly (dimethylsiloxane) and their chemical derivatives. *Langmuir*, **7**, 1013–1025.
- CHEN, D., WEAVERS, L.K. & WALKER, H.W. (2006). Ultrasonic control of ceramic membrane fouling by particles: Effect of ultrasonic factors. *Ultrason. Sonochem.*, **13**, 379–387.
- CHEN, H., LI, X., WAN, M. & WANG, S. (2009). High-speed observation of cavitation bubble clouds near a tissue boundary in high-intensity focused ultrasound fields. *Ultrasonics*, **49**, 289–292.

REFERENCES

- CHINI, S.F. & AMIRFAZLI, A. (2010). Understanding pattern collapse in photolithography process due to capillary forces. *Langmuir*, **26**, 13707–13714.
- COHEN, A.E. & MAHADEVAN, L. (2003). Kinks, rings, and rackets in filamentous structures. *Proc. Natl. Acad. Sci. U.S.A.*, **100**, 12141–12146.
- CRUM, L. (1979). Surface oscillations and jet development in pulsating bubbles. *J. Phys. Colloques*, **40**, C8–285–C288–288.
- CRUM, L.A. (1975). Bjerknes forces on bubbles in a stationary sound field. *J. Acoust. Soc. Am.*, **57**, 1363–1370.
- DEGUCHI, K., MIYOSHI, K., ISHII, T. & MATSUDA, T. (1992). Patterning characteristics of a chemically-amplified negative resist in synchrotron radiation lithography. *Jpn. J. Appl. Phys.*, **31**, 2954–2958.
- DELAMARCHE, E., SCHMID, H., MICHEL, B. & BIEBUYCK, H. (1997). Stability of molded polydimethylsiloxane microstructures. *Adv. Mater.*, **9**, 741–746.
- DIJKINK, R. & OHL, C.D. (2008). Measurement of cavitation induced wall shear stress. *Appl. Phys. Lett.*, **93**, 254107.
- DUAN, H. & BERGGREN, K.K. (2010). Directed self-assembly at the 10 nm scale by using capillary force-induced nanocoheion. *Nano Lett.*, **10**, 3710–3716.
- ELLER, A.I. & CRUM, L.A. (2005). Instability of the motion of a pulsating bubble in a sound field. *J. Acoust. Soc. Am.*, **47**, 762–767.
- FRANCESCUTTO, A. & NABERGOJ, R. (1978). Pulsation amplitude threshold for surface waves on oscillating bubbles. *Acta Acusti. United Ac.*, **41**, 215–220.

REFERENCES

- FUSI, M., DI FONZO, F., CASARI, C., MACCALLINI, E., CARUSO, T., AGOSTINO, R., BOTTANI, C. & LI BASSI, A. (2011). Island organization of tio_2 hierarchical nanostructures induced by surface wetting and drying. *Langmuir*, **27**, 1935–1941.
- GALLEGO-JUAREZ, J.A., RIERA, E., ACOSTA, V., RODRIGUEZ, G. & BLANCO, A. (2010). Ultrasonic system for continuous washing of textiles in liquid layers. *Ultrason. Sonochem.*, **17**, 234–238.
- GARNETT, E. & YANG, P. (2010). Light trapping in silicon nanowire solar cells. *Nano Lett.*, **10**, 1082–1087.
- GLASSMAKER, N., JAGOTA, A., HUI, C.Y. & KIM, J. (2004). Design of biomimetic fibrillar interfaces: 1. making contact. *J. R. Soc. Interface*, **1**, 23–33.
- GONZALEZ-AVILA, S.R., HUANG, X., QUINTO-SU, P.A., WU, T. & OHL, C.D. (2011). Motion of micrometer sized spherical particles exposed to a transient radial flow: attraction, repulsion, and rotation. *Phys. Rev. Lett.*, **107**, 074503.
- HENRY, M., WALAVALKAR, S., HOMYK, A. & SCHERER, A. (2009). Alumina etch masks for fabrication of high-aspect-ratio silicon micropillars and nanopillars. *Nanotechnology*, **20**, 255305.
- HICKLING, R. & PLESSET, M.S. (2004). Collapse and rebound of a spherical bubble in water. *Phys. Fluids.*, **7**, 7–14.
- HOLSTEYNS, F., LEE, K.T., GRAF, S., PALMANS, R., VEREECKE, G. & MERTENS, P.W. (2005). Megasonics: a cavitation driven process. *Solid State Phenom.*, **103**, 159–162.
- HOLT, R.G. & GAITAN, D.F. (1996). Observation of stability boundaries in the parameter space of single bubble sonoluminescence. *Phys. Rev. Lett.*, **77**, 3791.

REFERENCES

- HUI, C., LIN, Y., BANEY, J. & JAGOTA, A. (2000). The accuracy of the geometric assumptions in the jkr (johnsonkendallroberts) theory of adhesion. *J. Adhes. Sci. Technol.*, **14**, 1297–1319.
- HUI, C., JAGOTA, A., LIN, Y. & KRAMER, E. (2002). Constraints on microcontact printing imposed by stamp deformation. *Langmuir*, **18**, 1394–1407.
- ISHIDA, H., NUNTADUSIT, C., KIMOTO, H., NAKAGAWA, T. & YAMAMOTO, T. (2001). Cavitation bubble behavior near solid boundaries. *in Proceedings CAV2001 Fourth International Symposium on Cavitation, California Institute of Technology, Pasadena, CA.*
- JINCAO, Y., MATTHEWS, M.A. & DARVIN, C.H. (2001). Prevention of photoresist pattern collapse by using liquid carbon dioxide. *Ind. Eng. Chem. Res.*, **40**, 5858–5860.
- JOHNSON, K., KENDALL, K. & ROBERTS, A. (1971). Surface energy and the contact of elastic solids. *Proc. R. Soc. Lond. A*, **324**, 301–313.
- KENDALL, K. (1994). Adhesion: molecules and mechanics. *Science*, **263**, 1720–1725.
- KIM, C.H., YUN, M.S., HWANG, T.H., NAM, C.H., KIM, S.C., ROH, J.H., LEE, M.S. & AN, J.S. (2013). Improved drying technology of single wafer tool by using hot ipa/diw. *Solid State Phenom.*, **195**, 243–246.
- KIM, G.H., CHO, S.H., HAN, J.H., LEE, Y.B., ROH, C.H., HONG, K. & PARK, S.K. (2012). Effect of drying liquid on stiction of high aspect ratio structures. *Solid State Phenom.*, **187**, 75–78.
- KIM, H.Y. & MAHADEVAN, L. (2006). Capillary rise between elastic sheets. *J. Fluid Mech.*, **548**, 141–150.

REFERENCES

- KIM, T.H. & KIM, H.Y. (2014). Disruptive bubble behaviour leading to microstructure damage in an ultrasonic field. *J. Fluid Mech.*, **750**, 355–371.
- KIM, W., KIM, T.H., CHOI, J. & KIM, H.Y. (2009). Mechanism of particle removal by megasonic waves. *Appl. Phys. Lett.*, **94**, 081908.
- KIM, W., PARK, K., OH, J., CHOI, J. & KIM, H.Y. (2010). Visualization and minimization of disruptive bubble behavior in ultrasonic field. *Ultrasonics*, **50**, 798–802.
- KONDO, T., JUODKAZIS, S. & MISAWA, H. (2005). Reduction of capillary force for high-aspect ratio nanofabrication. *Appl. Phys. A*, **81**, 1583–1586.
- KORNFELD, M. & SUVOROV, L. (1944). On the destructive action of cavitation. *J. Appl. Phys.*, **15**, 495–506.
- LAMB, H. (1993). *Hydrodynamics*. Cambridge university press.
- LAMMINEN, M.O., WALKER, H.W. & WEAVERS, L.K. (2004). Mechanisms and factors influencing the ultrasonic cleaning of particle-fouled ceramic membranes. *J. Membr. Sci.*, **237**, 213–223.
- LAUTERBORN, W. & HENTSCHEL, W. (1985). Cavitation bubble dynamics studied by high speed photography and holography: part one. *Ultrasonics*, **23**, 260–268.
- LAUTERBORN, W. & OHL, C.D. (1997). Cavitation bubble dynamics. *Ultrason. Sonochem.*, **4**, 65–75.
- LEE, T.W., MITROFANOV, O. & HSU, J.W. (2005). Pattern-transfer fidelity in soft lithography: The role of pattern density and aspect ratio. *Adv. Funct. Mater.*, **15**, 1683–1688.
- LEIGHTON, T. (1994). *The Acoustic Bubble*. Academic press.

REFERENCES

- LINDAU, O. & LAUTERBORN, W. (2003). Cinematographic observation of the collapse and rebound of a laser-produced cavitation bubble near a wall. *J. Fluid Mech.*, **479**, 327–348.
- METTIN, R., AKHATOV, I., PARLITZ, U., OHL, C. & LAUTERBORN, W. (1997). Bjerknes forces between small cavitation bubbles in a strong acoustic field. *Phys. Rev. E*, **56**, 2924.
- MINNAERT, M. (1933). On musical air-bubbles and the sounds of running water. *Phil. Mag.*, **16**, 235–248.
- NAMATSU, H., YAMAZAKI, K. & KURIHARA, K. (1999). Supercritical drying for nanostructure fabrication without pattern collapse. *Microelectron. Eng.*, **46**, 129–132.
- NAUDE, C.F. & ELLIS, A.T. (1961). On the mechanism of cavitation damage by nonhemispherical cavities collapsing in contact with a solid boundary. *Tran. ASME D: J. Basic Eng.*, **83**, 648–656.
- OHL, C.D., KURZ, T., GEISLER, R., LINDAU, O. & LAUTERBORN, W. (1999). Bubble dynamics, shock waves and sonoluminescence. *Phil. Trans. R. Soc. Lond. A*, **357**, 269–294.
- PECHA, R. & GOMPF, B. (2000). Microimplosions: cavitation collapse and shock wave emission on a nanosecond time scale. *Phys. Rev. Lett.*, **84**, 1328–1330.
- PHILIPP, A. & LAUTERBORN, W. (1998). Cavitation erosion by single laser-produced bubbles. *J. Fluid Mech.*, **361**, 75–116.
- POKROY, B., EPSTEIN, A.K., PERSSON-GULDA, M. & AIZENBERG, J. (2009a). Fabrication of bioinspired actuated nanostructures with arbitrary geometry and stiffness. *Adv. Mater.*, **21**, 463–469.

REFERENCES

- POKROY, B., KANG, S.H., MAHADEVAN, L. & AIZENBERG, J. (2009b). Self-organization of a mesoscale bristle into ordered, hierarchical helical assemblies. *Science*, **323**, 237–240.
- PRABOWO, F. & OHL, C.D. (2011). Surface oscillation and jetting from surface attached acoustic driven bubbles. *Ultrason. Sonochem.*, **18**, 431–435.
- SADER, J.E. (1998). Frequency response of cantilever beams immersed in viscous fluids with applications to the atomic force microscope. *J. Appl. Phys.*, **84**, 64–76.
- SCHNEIDER, F., FELLNER, T., WILDE, J. & WALLRABE, U. (2008). Mechanical properties of silicones for mems. *J. Micromech. Microeng.*, **18**, 065008.
- SHAW, S. & SPELT, P. (2010). Shock emission from collapsing gas bubbles. *J. Fluid Mech.*, **646**, 363–373.
- SHIBATA, T., ISHII, T., NOZAWA, H. & TAMAMURA, T. (1997). High-aspect-ratio nanometer-pattern fabrication using fullerene-incorporated nanocomposite resists for dry-etching application. *Jpn. J. Appl. Phys.*, **36**, 7642–7645.
- SHIMA, A., TAKAYAMA, K., TOMITA, Y. & OHSAWA, N. (1983). Mechanism of impact pressure generation from spark-generated bubble collapse near a wall. *AIAA J.*, **21**, 55–59.
- SHUTLER, N.D. & MESLER, R. (1965). A photographic study of the dynamics and damage capabilities of bubbles collapsing near solid boundaries. *Tran. ASME D: J. Basic Eng.*, **87**, 511–517.
- SUWITO, W., DUNN, M.L., CUNNINGHAM, S.J. & READ, D.T. (1999). Elastic moduli, strength, and fracture initiation at sharp notches in

REFERENCES

- etched single crystal silicon microstructures. *J. Appl. Phys.*, **85**, 3519–3534.
- TANAKA, T., MORIGAMI, M. & ATODA, N. (1993). Mechanism of resist pattern collapse during development process. *Jpn. J. Appl. Phys.*, **32**, 6059–6064.
- TANAKA, T., MORIGAMI, M., OIZUMI, H., OGAWA, T. & UCHINO, S.I. (1994a). Prevention of resist pattern collapse by flood exposure during rinse process. *Jpn. J. Appl. Phys.*, **33**.
- TANAKA, T., MORIGAMI, M., OIZUMI, H., SOGA, T., OGAWA, T. & MURAI, F. (1994b). Prevention of resist pattern collapse by resist heating during rinsing. *J. Electrochem. Soc.*, **141**, L169–L171.
- TIMOSHENKO, S.P. & GOODIER, J.N. (1970). *Theory of Elasticity*. McGraw-Hill, New York.
- TOMITA, H., INUKAI, M., UMEZAWA, K. & JI, L.N. (2009). Direct observation of single bubble cavitation damage for mhz cleaning. *Solid State Phenom.*, **145**, 3–6.
- TOMITA, Y. & SHIMA, A. (1986). Mechanisms of impulsive pressure generation and damage pit formation by bubble collapse. *J. Fluid Mech.*, **169**, 535–564.
- VERSLUIS, M., GOERTZ, D.E., PALANCHON, P., HEITMAN, I.L., VAN DER MEER, S.M., DOLLET, B., DE JONG, N. & LOHSE, D. (2010). Microbubble shape oscillations excited through ultrasonic parametric driving. *Phys. Rev. E*, **82**, 026321.
- VOGEL, A., LAUTERBORN, W. & TIMM, R. (1989). Optical and acoustic investigations of the dynamics of laser-produced cavitation bubbles near a solid boundary. *J. Fluid Mech.*, **206**, 299–338.

REFERENCES

- WAGTERVELD, R., BOELS, L., MAYER, M. & WITKAMP, G. (2011). Visualization of acoustic cavitation effects on suspended calcite crystals. *Ultrason. Sonochem.*, **18**, 216–225.
- WU, B., KUMAR, A. & PAMARTHY, S. (2010). High aspect ratio silicon etch: A review. *J. Appl. Phys.*, **108**, 051101.
- YAWS, C.L. (1999). *Chemical Properties Handbook*. McGraw-Hill, New York.
- YU, M.F., KOWALEWSKI, T. & RUOFF, R.S. (2001). Structural analysis of collapsed, and twisted and collapsed, multiwalled carbon nanotubes by atomic force microscopy. *Phys. Rev. Lett.*, **86**, 87.
- ZHANG, Y., LO, C.W., TAYLOR, J.A. & YANG, S. (2006). Replica molding of high-aspect-ratio polymeric nanopillar arrays with high fidelity. *Langmuir*, **22**, 8595–8601.

국 문 초 록

반도체 초음파 세정 및 건조과정에서 발생하는 미세구조물 손상에 대한 연구

본 연구는 반도체 세정과정에서 초음파 기포나 증발하는 액막과 미세 구조물과의 상호작용에 대하여 다루었다. 특히, 미세구조물의 손상과정을 직접관찰하고 그것을 바탕으로 미세구조물의 손상을 최소화하는 방법을 찾는 데 주안점을 두었다.

반도체세정 과정은 미세구조물 제작과정에서 발생하는 오염입자를 초음파에 의한 버블 진동을 이용하여 제거하고, 세정과정에 사용된 세정액을 깨끗한 물로 행구어 건조시키는 일련의 과정으로 이루어져 있다. 이때 초음파에 의하여 발생한 기포들의 파괴적인 운동으로 오염입자뿐만 아니라 미세구조물에도 큰 충격이 가해져 구조물이 부서지거나, 건조하는 과정에서 액체의 모세관힘에 의하여 패턴들이 서로 달라붙는 패턴 손상 현상이 빈번하게 나타나고 있다. 따라서 본 연구에서는 반도체 세정과정 중 발생하는 패턴손상을 1) 초음파 세정에서 파괴적인 초음파 버블에 의한 구조물 손상과 2) 건조과정에서 증발하는 액막에 의한 패턴 붙음현상으로 나누어 진행하였다.

버블의 진동은 반도체 웨이퍼, 포토마스크, 멤브레인 등 고체표면에 붙은 오염입자를 제거하는 초음파세정에서 중요한 역할을 하고 있다. 하지만 강한 버블의 진동은 미세구조물의 크기가 점점 작아짐에 따라 오염입자뿐만 아니라 구조물 자체에도 큰 충격을 가하여 패턴이 손상되는 결과를 초래하고 있다. 따라서 본 연구에서는 초고속

카메라를 이용하여 패턴과 상호작용을 하는 미세버블에 대하여 관찰하고 이를 바탕으로 버블의 운동을 네 가지로 분류(부피진동, 형상진동, 분리운동, 무작위진동)하였다. 또한, 실험조건에 따라 버블운동을 예측하는 지도(regime map)를 만들어, 각 운동의 특성을 파악하고 실제 미세구조물에 손상을 주는 버블의 양상을 관찰하여 버블의 크기가 작을 때는 분리운동으로 구조물에 손상을 가하고, 버블의 크기가 클 때는 파괴적인 무작위적인 운동으로 미세구조물에 손상을 야기시킨다는 것을 밝혔다.

건조과정은 세정과정 중 가장 마지막 단계로 액막이 증발함에 따라 액체계면이 미세구조물 끝에 걸리고 액체계면과 고체표면 사이 모세관힘(capillary force)에 의하여 구조물을 끌어당겨 구조물들이 서로 달라붙는 패턴 붙음현상이 발생한다. 본 연구에서는 마이크로 스케일의 탄성 폴리머 패턴들을 만들어 액막이 증발함에 따라 패턴과 액막사이 나타나는 탄성모세관(elastocapillary)현상을 가시화하고, 간단한 모델을 이용하여 패턴들이 붙는 현상을 예측하였다. 또한 패턴의 표면온도 변화를 통하여 패턴사이 액막의 증발양상 변화를 이용하여 미세구조물 붙음현상을 최소화하는 방법을 실험적으로 밝혔다.

본 연구는 반도체 세정과정 중 발생하는 미세패턴 손상에 대하여 그 현상을 직접 관찰하여 패턴손상에 대한 물리적 이해를 도우며, 관찰한 결과를 바탕으로 미세패턴 손상을 최소화 시킬 수 있는 방법에 대하여 제시하였다.

주요어 : 패턴손상, 초음파세정, 미세기포, 탄성모세관, 표면에너지.

학 번 : 2010-30184